ELSEVIER

Contents lists available at ScienceDirect

Materials Science & Engineering A

journal homepage: www.elsevier.com/locate/msea





Fracture toughness and fatigue crack growth resistance of precipitate-free and precipitation hardened NiTiHf shape memory alloys

Benjamin Young ^{a, 1}, Roberto Orrostieta ^{a, 1}, Behrouz Haghgouyan ^a, Dimitris C. Lagoudas ^{a, b}, T. Baxevanis ^c, Ibrahim Karaman ^{a, b, *}

- ^a Department of Materials Science & Engineering, Texas A&M University, College Station, TX, 77843, USA
- ^b Department of Aerospace Engineering, Texas A&M University, College Station, TX, 77843, USA
- ^c Department of Mechanical Engineering, University of Houston, Houston, TX, 77204-4006, USA

ARTICLE INFO

Keywords: Fatigue crack growth Martensitic transformation High-temperature shape memory alloys NiTiHf Precipitation hardening

ABSTRACT

The present work investigates fracture toughness, and actuation and mechanical fatigue crack growth responses of $\mathrm{Ni}_{50.3}\mathrm{Ti}_{29.7}\mathrm{Hf}_{20}$ HTSMAs across martensitic transformation with two different microstructures, one with H-phase nanoprecipitates and one without. H-phase precipitation is known to stabilize the actuation cycling response of NiTiHf HTSMAs and notably impacts transformation-induced plasticity. The fracture toughness tests performed reveal that precipitate-free NiTiHf has a higher fracture toughness and undergoes significantly more inelastic deformation than the one with the precipitates resulting in toughness enhancement, i.e., stable crack advance during fracture toughness experiments, which is not observed in the precipitated NiTiHf for the crack configuration and loading conditions tested. Furthermore, the precipitate free NiTiHf has higher actuation and mechanical fatigue crack growth resistance than the precipitation-hardened microstructure. This is attributed to plasticity buildup, which exacerbates the manifestation of retained martensite upon repeated transformations. The fatigue crack growth rates obtained from both actuation and mechanical fatigue experiments align to a single Paris Law Curve for the precipitation-hardened NiTiHf. This work aims to determine if unified Paris Law curves can be generated from mechanical and actuation fatigue experiments, irrespective of composition and microstructure, to estimate actuation fatigue crack growth rates, laborious and challenging to measure, from easier to detect mechanical fatigue crack growth rates.

1. Introduction

Shape memory alloys (SMAs) are a class of active materials capable of high-power solid-state actuation — a desirable functional characteristic for a wide range of applications [1]. Among the different types of SMAs, high-temperature shape memory alloys (HTSMAs) are of great interest since they can be used as actively controlled solid-state actuators at temperatures above 100 °C [2]. As such, HTSMA–actuators are envisioned in aerospace and automotive applications under extreme environments of up to 500 °C [2]. To achieve such high transformation temperatures (TTs), NiTi-based ternary alloys, NiTiX (X = Au, Pt, Pd, Zr, or Hf), have been developed [2,3]. Hf has been proven as one of the better alternatives for ternary HTSMAs [3,4] since Au, Pt, and Pd are cost-prohibitive and NiTiZr is thermally unstable as compared to NiTiHf [5]. As a result, many studies have been performed to optimize the

properties and performance of NiTiHf system [6-30].

Unlike NiTi, where several reviews [31–34] present the large body of fracture mechanics literature for this material, research on NiTiHf HTSMAs has mainly focused on functional fatigue [20–22,35–37] while only a limited number of studies have been performed on the fracture mechanics of NiTiHf in the presence of martensitic transformation [38–41]. Functional fatigue has been given much focus for volume and mass limited applications where macro crack growth rates occupy a short fraction of the applications' active life [31]. In SMAs, actuation and superelastic functional fatigue can be interpreted as total life approaches (i.e., S–N cycling) since these experiments investigate the crack nucleation and subsequent failure of SMAs due to cyclic martensitic transformation when there are no stress concentrators in the testing specimens. Moreover, although crack nucleation is permissible in total life testing, these types of experiments seek to determine material loading conditions in which microcrack arresting can occur before

^{*} Corresponding author. Department of Materials Science & Engineering, Texas A&M University, College Station, TX 77843, USA. *E-mail address:* ikaraman@tamu.edu (I. Karaman).

 $^{^{1}\,}$ These authors contributed equally.

Nomenclature		P_{max}	Maximum applied load during mechanical fatigue crack growth cycling
а	Crack length	P_{min}	Minimum applied load during mechanical fatigue crack
A^{CMOD}	Total area under a load-crack mouth opening displacement		growth cycling
	(CMOD) plot	R	Ratio of maximum-to-minimum applied load during
A^{el}	Area corresponding to the elastic regime under a load-		mechanical fatigue crack growth cycling $\left(rac{P_{min}}{P_{max}} ight)$
A^{in}	displacement plot Area corresponding to the inelastic regime under a load-	$V^{LLD,el}$	Elastic component of displacement at the LLD point
A	displacement plot	$V^{LLD,in}$	Inelastic component displacement at the LLD point
A^{LLD}	Total area under a load-load line displacement (LLD) plot	V^{CMOD}	Displacement at the CMOD point
A_f	Austenite finish temperature	V^{LLD}	Displacement at the LLD point
a_o	Initial/precracked crack length	V_{max}^{LLD}	Displacement after full martensitic transformation (i.e.,
A_s	Austenite start temperature		cooling) during actuation crack growth cycling
В	CT specimen thickness (as per ASTM 1820)	V_{min}^{LLD}	Displacement after full austenitic transformation (i.e.,
b	CT's unbroken ligament		heating) during actuation crack growth cycling
C	Compliance as determined using the inverse slope of a	W	CT specimen width (as per ASTM 1820)
	load-displacement plot	ΔJ^{el}	Change in the elastic component of stress intensity factor <i>J</i>
$C^{LLD,unloa}$	ding LLD compliance determined by using the linear segment	. Tin	during a mechanical/actuation fatigue crack growth cycle
	of a load-LLD mechanical cycle plot during unloading	ΔJ^{in}	Change in the inelastic component of stress intensity factor
C^{CMOD}	Compliance as determined using the inverse slope of a		J during a mechanical/actuation fatigue crack growth
IID	load-CMOD plot	ΔJ	cycle Change in stress intensity <i>J</i> corresponding maximum and
C^{LLD}	Compliance as determined using the inverse slope of a	Δυ	minimum <i>J</i> values during a mechanical/actuation fatigue
oIID	load-LLD plot		crack growth cycle
C_{Aus}^{LLD}	Compliance as determined using the inverse slope of a	$\Delta V^{LLD,el}$	Change between the maximum and minimum elastic
	load-LLD plot in the austenite phase during actuation crack growth cycling		component displacement values at the LLD point during a
C_{Mar}^{LLD}	Compliance as determined using the inverse slope of a		mechanical/actuation fatigue crack growth cycle
G _{Mar}	load-LLD plot in the martensite phase during actuation	$\Delta V^{LLD,in}$	Change between the maximum and minimum inelastic
	crack growth cycling		component displacement values at the LLD point during a
<u>da</u> dN	Change in crack length per mechanical/actuation cycle		mechanical/actuation fatigue crack growth cycle
dN . J	Elastic-plastic fracture mechanics (EPFM) stress intensity	ΔV^{LLD}	Change between the maximum and minimum
J	factor		displacement values at the LLD point during a mechanical/
J^{el}	Elastic-plastic fracture mechanics (EPFM) stress intensity		actuation fatigue crack growth cycle
	factor corresponding to energy dissipated by the elastic	Δa	Crack extension
	response of a compact tension (CT) specimen	ΔA^{el}	Elastic area under a load-displacement plot resulting from
J^{in}	EPFM stress intensity factor corresponding to energy	ΔA^{in}	a mechanical or actuation fatigue crack growth cycle
	dissipated by the inelastic response of a CT specimen	ΔA^{m}	Inelastic area under a load-displacement plot resulting from a mechanical or actuation fatigue crack growth cycle
M_d	Martensite desist temperature	ΔP	Maximum minus minimum applied load during cycling
M_f	Martensite finish temperature	Δ1	$(P_{max} - P_{min})$
M_s	Martensite start temperature	γ^{el}	Geometric factor constant used to determine J^{el}
P_{bias}	Constant applied load during actuation crack growth	γ^{in}	Geometric factor constant used to determine J^{in} .
D.	cycling The maximum lead just prior to ith unleading step during	η^{el}	Geometric factor constant used to determine J^{el}
P_i	The maximum load just prior to ith unloading step during fracture toughness testing	η^{in}	Geometric factor constant used to determine J^{in}
	nactare toughness testing		

macrocracks and stable crack growth appear. In general, deteriorated functional fatigue resistance has been observed in NiTiHf with decreasing Ni content [37], increasing upper cycle temperatures (UCT) [20,35], and/or increasing bias load [20,21]. In addition, microstructure features such as non-metallic inclusions lower the functional fatigue life [37] while H-phase nanoprecipitates stabilize transformation temperatures NiTiHf [16,37].

On the other hand, the defect tolerant design assumes that the material inherently has defects (e.g., inclusions) that act as stress raisers which can lead to macrocrack formation followed by steady crack growth. Hence, due to the assumption of the inherent presence of defects, defect tolerant design is more conservative and preferred in highrisk fields such as aerospace, defense, energy industry, and building infrastructure, where the larger size of actuation components enables permissible crack growth before the components must be retired. Recent results of defect tolerant design experiments in NiTiHf include fracture toughness, mechanical crack growth (i.e. force/stress cycling at nomi-

nally constant temperatures), and actuation crack growth (thermal cycling under constant force/stress). Fracture toughness experiments on NiTiHf conducted by Young et al. [38] revealed that in the absence of H-phase precipitates, martensitic transformation in NiTiHf acts as a toughening mechanism. The highest fracture toughness values, attained just above the M_s temperature, were attributed to the larger inelastic zone generated by the combination of austenite plasticity, stress induced martensite (SIM), martensite detwinning, and the unequal strain hardening of the austenite and martensite phases. Haghgouyan et al. [39] first performed fracture toughness in nanoprecipitation hardened (in peak aged condition after 550 °C 3h heat treatment) Ni_{50.3}Ti_{29.7}Hf₂₀ at room temperature, for which brittle failure response was observed. Follow up studies by Haghgouyan et al. [41] investigated the mechanical and actuation fatigue crack growth behavior of nanoprecipitation hardened Ni_{50 3}Ti_{29 7}Hf₂₀; these crack growth results will be juxtaposed with the results attained in this work. More recently, actuation crack growth was investigated by Ekiciler et al. in NiTiHf single edge notch

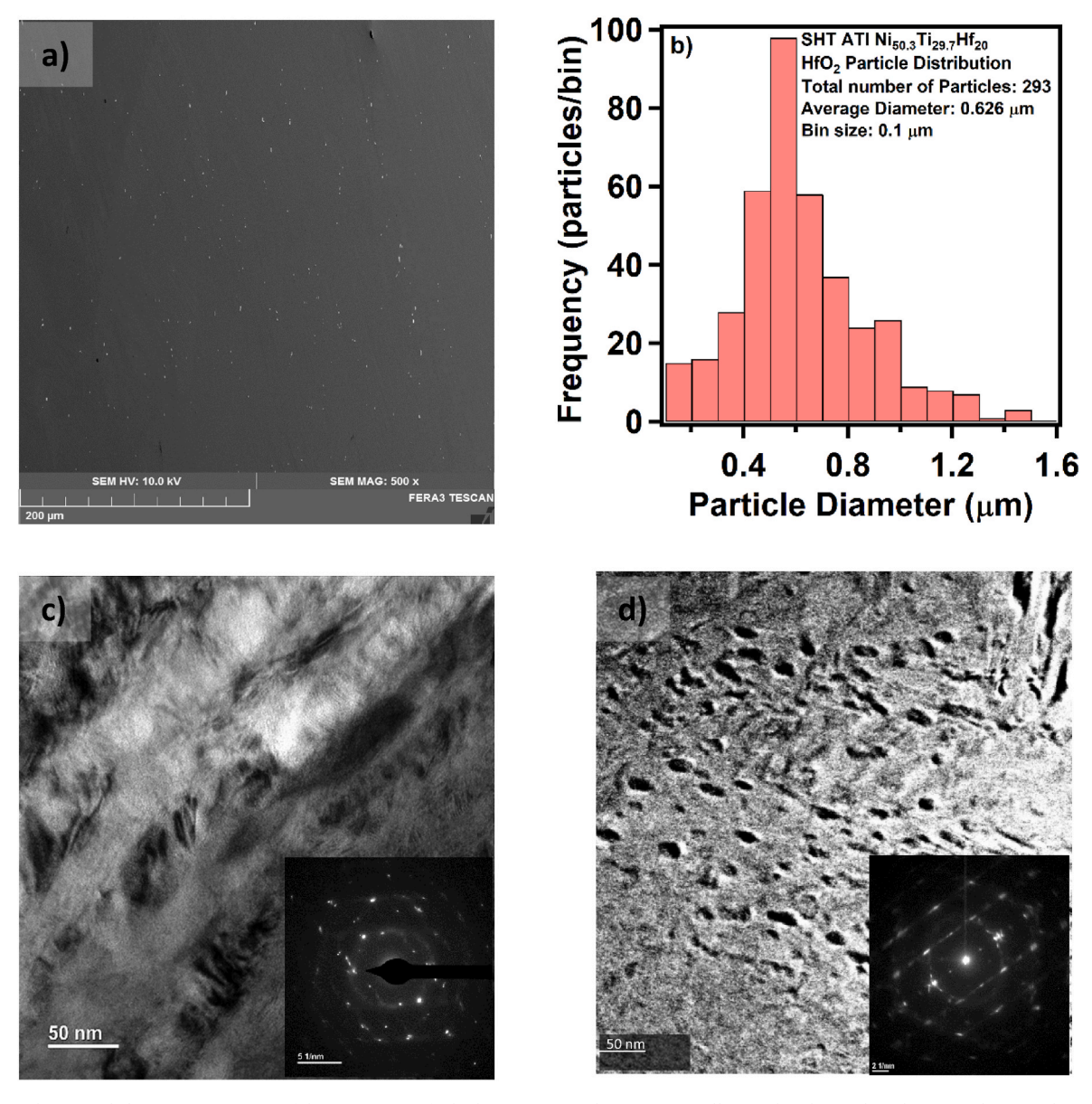


Fig. 1. (a) Backscattered electron (BSE) image of the $Ni_{50.3}$ Ti_{29.7}Hf₂₀ high temperature shape memory alloy used in this study. White particles were determined to be HfO_2 from wavelength dispersive spectroscopy (WDS) measurements. The size and distribution of these particles can be seen in (b). When the material is solutionized for 1 h at 900 °C under argon atmosphere, the microstructure is precipitate-free, (c). After an aging heat treatment of 550 °C for 3 h under argon atmosphere, coherent H-phase nano-precipitates form, seen in (d).

tension (SENT) specimens under two conditions: hot-extruded and annealed conditions [40]. In this work, a steady increment in irrecoverable strain and crack length was observed with actuation cycling prior to failure of both sample conditions. Nonetheless, a stable actuation strain was achieved after ~800 cycles under a 200 MPa bias load. Finally, fractography revealed microcracking as a toughening mechanism since side cracks emanated adjacent to a main crack at the notch [40].

Despite these findings, insufficient understanding of the effects of cyclic martensitic transformations on their structural degradation and fatigue crack behavior has hindered HTSMAs' use in applications where cyclic actuation is required [42,43]. This is partly caused by the complications arising from reversible martensitic transformations in the entire sample upon actuation cycling in the presence of defects/cracks, accompanying inelastic deformation modes, repeated changes in elastic properties at the crack tip during crack growth, and limitations of Linear Elastic Fracture Mechanics (LEFM) and Elastic-Plastic Fracture Mechanics (EPFM) approaches employed to analyze actuation fatigue crack

growth experiments. Hence, a modified Paris Law approach, based on the *J*-integral, was proposed by the authors to account for the inelastic response and elastic property changes accompanying martensitic transformation during actuation cycling [41]. Moreover, the authors have proposed a mechanics-aided test method for measuring the fracture toughness of SMAs, whose deformation/failure response violates basic assumptions of ASTM standards for measuring fracture toughness in conventional ductile materials [38,39,44,45].

Adopting these methodologies, the present work focuses on elucidating the role of solution heat treated (SHT) (i.e., precipitate-free) and peak aged (PA) (i.e., with coherent H-phase nanoprecipitates) microstructures in Ni_{50.3}Ti_{29.7}Hf₂₀ HTSMAs during fracture toughness, mechanical and actuation fatigue crack growth experiments. Fracture toughness experiments are performed at three distinct temperatures: (i) below the martensite-finish temperature, M_f ; (ii) between the martensite-start temperature, M_s , and the martensite desist temperature, M_d , above which the stress-induced martensitic transformation is suppressed; and (iii) above M_d . At these temperatures, the material either

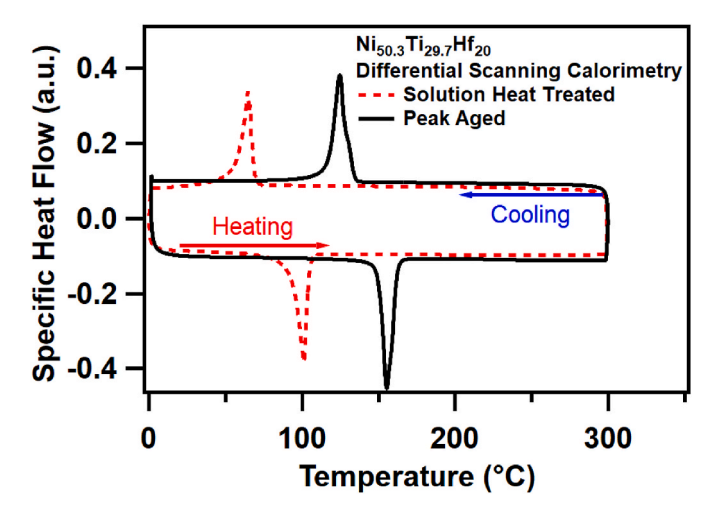


Fig. 2. Differential scanning calorimetry curves of the $Ni_{50.3}Ti_{29.7}Hf_{20}$ HTSMA showing transformation temperatures of Peak Aged, with precipitates (black, solid line), and the Solution Heat Treated, precipitate-free microstructure (red, dashed line). (For interpretation of the references to colour in this figure legend, the reader is referred to the Web version of this article.)

remains in the martensite state throughout the loading/unloading intervals (case (i)), transforms from austenite to martensite close to the crack tip (case (ii)), or remains always in the austenite state (case (iii)).

In this study, it will be shown that a single Paris Law type $\left(\frac{da}{dN}vs\Delta J\right)$ curve can be obtained from isobaric actuation and near-isothermal mechanical loading paths for the PA material, which offers the possibility of reducing the time and cost of actuation testing by performing significantly faster mechanical cycling experiments to predict the crack growth rates under actuation loading. Precipitate-free NiTiHf also shows continuity as a single Paris curve. However, continuous crack growth is observed near the unstable crack growth regime of the Paris curve, thus the prediction of stable actuation crack growth with mechanical cycling in precipitate free NiTiHf is rather inconclusive.

2. Materials and methods

2.1. Materials

A multiple vacuum arc (VAR) melted, hot extruded Ni $_{50.3}$ Ti $_{29.7}$ Hf $_{20}$ (nominal, at.%) round bar was acquired from ATI Metals. To produce the SHT and PA microstructures, the material was first solution heat treated (SHT) at 900 °C for 1 h under inert atmosphere followed by water quenching to dissolve any second-phase particles that may have formed during the extrusion process. Some of the SHT material was then subjected to a peak aging (PA) at 550 °C for 3 h under inert atmosphere followed by water quenching. This treatment creates coherent H-phase nanoprecipitates [46], which are known to yield stable reversibility of martensitic transformation [22] in this alloy within the desired transformation temperature range.

2.2. Microstructural and thermal characterization

The microstructure of the materials was characterized using scanning electron microscopy (SEM), wavelength dispersive spectroscopy (WDS) analysis, and transmission electron microscopy (TEM). Secondary electron (SE) and backscattered electron (BSE) images were obtained using a Tescan Fera3 SEM with an accelerating voltage of 20 kV. The BSE samples were prepared via mechanical grinding with abrasive papers up to 1200 grit, and then further polished using a colloidal silica suspension on a vibratory polisher. TEM images were acquired using a FEI Tecnai G2 F20 TEM with an accelerating voltage of 200 kV. TEM samples were mechanically ground with 1000 grit abrasive paper down

to a thickness of 80 μ m followed by twin-jet polishing using a 20% HNO₃ and 80% methanol solution at -20 °C under 11 V. Backscattered electron images (Fig. 1a) reveal white secondary-phase particles that are identified as HfO₂. The composition of these particles was confirmed with WDS. The size and distribution of the HfO₂ particles is shown in Fig. 1b. Fig. 1c displays the bright field TEM image of the SHT samples, captured on the [100] zone axis of the B19' martensitic phase, without any precipitates. Fig. 1d shows the bright-field TEM image where the coherent H-phase nano-precipitates are located within individual martensite variants. These precipitates are small (10–20 nm), and therefore do not stop the martensite phase front propagation, as they are absorbed by the martensite variants during transformation [46].

Transformation temperatures (TTs) were measured using a TA Instruments Q2000 differential scanning calorimeter (DSC) with a heating/cooling rate of 10 °C/min from 0 to 300 °C. The transformation temperatures (martensite finish (M_f), martensite start (M_s), austenite start (A_s), and austenite finish (A_f), respectively) were found to be 55, 69, 93, and 105 °C in SHT samples, and 118, 134, 150, and 163 °C in PA samples. This increase of transformation temperatures in PA samples is expected because the formation of H-phase precipitates during aging results in a relatively more nickel-lean matrix than in the SHT material. The DSC curves for the samples for both microstructures can be found in Fig. 2. The procedure to determine M_d is described in the following subsection.

2.3. Uniaxial tensile experiments

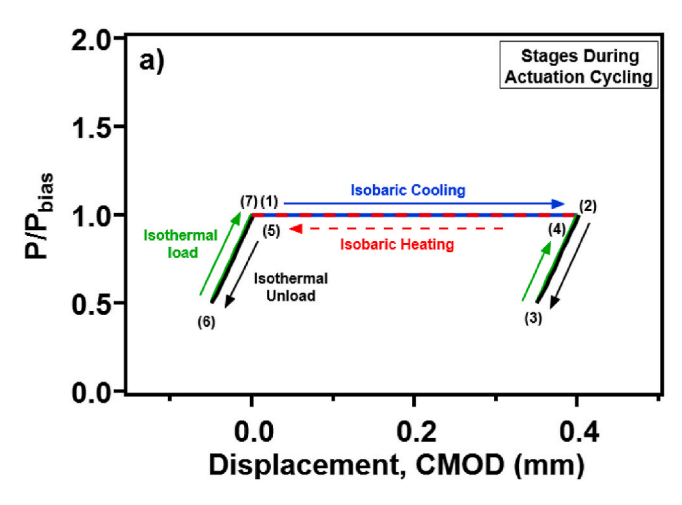
Flat dog-bone shaped specimens with gauge dimensions of $8\times3\times1$ mm 3 were machined using wire electro-discharge machining (EDM). Uniaxial tension experiments were performed on a servo-hydraulic MTS load frame equipped with a high-temperature MTS extensometer directly attached to the gauge section of the sample. Specimens were cut with their tensile axis perpendicular to the bar's concentric axis. Temperature was measured with a K-type thermocouple in contact with the specimen.

For isobaric heating cooling (IHC) experiments, the specimens were first heated under a small load to the upper cycle temperature (UCT) of $A_f+150\,^{\circ}\mathrm{C}$. Upon reaching UCT, the load on the specimen was increased to the next stress level and thermally cycled between the UCT, above A_f , and the lower cycle temperature (LCT), below M_f , at a rate of $10\,^{\circ}\mathrm{C/min}$, at loads corresponding to stresses of 50, 100, 150, 200, 300, 400, and 500 MPa.

Monotonic tension specimens were mechanically loaded until failure at a strain rate of $5 \times 10^{-4} \, \mathrm{s}^{-1}$. The testing temperatures were chosen based on the transformation temperatures (TTs) of NiTiHf so that the fully martensite, fully austenite, and stress-induced martensitically transforming austenite phases of the material would be tested. For experiments above M_s but below M_d , the specimens were first heated above A_f and then cooled to the test temperature under low load to ensure that full stress-induced martensitic (SIM) transformation would take place upon loading.

2.4. Fracture toughness and fatigue crack growth experiments

Following the ASTM Standard E1820 [47], the disk-shaped compact tension (DCT) specimens, with the width W=20 mm and the thickness $B=3.15\pm0.25$ mm, were cut from the bar for fracture toughness and fatigue crack growth experiments. Specimens were cut such that the loading direction for Mode I Crack growth is perpendicular to the bar's concentric axis. Both sides of the sample were prepared by mechanical grinding with abrasive papers to 1200 grit and vibratory polishing with a colloidal silica suspension to remove the wire EDM layer and have a better surface for optical crack measurements. All samples were fatigue pre-cracked and tested using a servo-hydraulic MTS test frame (MTS-810) with a 10 kN Interface load cell. Pre-cracking was performed



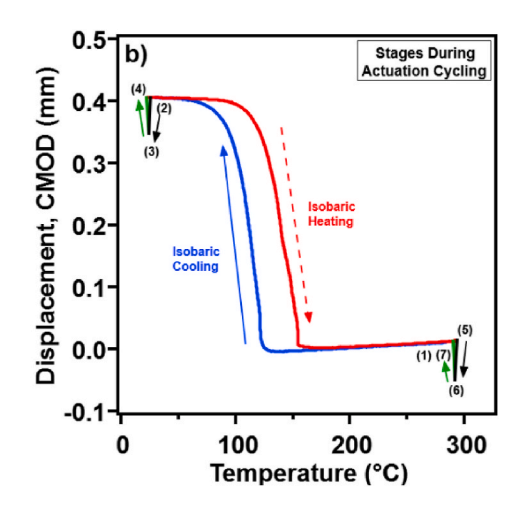


Fig. 3. (a) Schematic illustrating the stages in an actuation cycle beginning at (1) by holding the specimen at P_{bias} and at high temperature (above A_f) followed by isobaric cooling to point (2). Once the temperature stabilizes (below M_f), unload to point (3) and reload back to (4) is performed to determine the martensite phase compliance, and the specimen is subsequently heated at a constant P_{bias} load to point (5) (i.e., isobaric heating). Similarly, after the temperature stabilizes at the target temperature (above A_f), unload (point (6)) and reload is performed to determine the compliance of the austenite phase. (b) CMOD vs. temperature (°C) schematic illustrating the 6 stages of an actuation cycle through complete martensitic transformation and the partial unloads after completion of the phase transformation.

at room temperature under a cyclic, sinusoidal waveform at a frequency of 10 Hz and constant load ratio $R = \frac{P_{min}}{P_{max}} = 0.1$. During pre-cracking, the crack was optically monitored from both sides of the specimen until the desired initial crack size (a_o) was obtained. The temperature of the experiments was monitored with six K-type thermocouples spots welded to the specimen at different locations. Specimens were heated through induction with an Ambrell EasyHeat0224 with a custom copper workpiece controlled by a Eurotherm 2200 PID controller and cooled with assisted convection. Temperatures were recorded in a LabVIEW program through a Measurement Computing data acquisition board. Crack mouth opening displacement (CMOD), as defined by Newman et al. in Ref. [48] and ASTM E399 [49], was measured for all specimens with an MTS CMOD gauge.

For fracture toughness experiments, specimens were loaded in displacement control at a rate of 7.5×10^{-3} mm/s, per the procedure in ASTM Standard E1820 [47]. To capture specimen compliance during loading, a sequence of partial unload-reloads were performed by decreasing the displacement by 0.05 mm at 0.15 mm intervals. Both load and CMOD were measured at a rate of 10Hz throughout the experiments. For experiments above room temperature, the samples were heated with the induction heating setup previously mentioned. Similar to the uniaxial tension experiments at temperatures $M_s < T < M_d$, the specimens were first heated above A_f and then cooled to the test temperature under low load to ensure that stress-induced martensitic transformation would occur at the crack tip upon loading in mechanical fatigue growth experiments.

Mechanical fatigue crack growth experiments were conducted, according to the procedure described in ASTM E647 [50], at M_s +45 °C to ensure full reverse transformation at the crack tip upon unloading. The fatigue crack growth experiment was conducted under load control where the specimen is cycled under a sinusoidal waveform at a frequency of 10 Hz and constant load ratio R=0.1. To approach the threshold values, a load-shedding procedure was used until crack growth rates reached 10^{-10} m/cycle. For higher mechanical fatigue crack growth rates, a constant load scheme was adopted where P_{min} and P_{max} were held constant to move towards the unstable crack growth regime. The crack size was measured optically from both sides of the samples throughout the test. The imaging equipment consisted of a Point Grey Blackfly S camera with a Basler C11-1620-12M — P f16mm lens, resulting in a resolution of 20 μ m/pixel.

Actuation fatigue crack growth experiments are performed by ther-

Table 1List of coefficients used in Newman's displacement translation equation [48].

j	A_j^{CMOD}	A_j^{LLD}
1	0.26	1.742
2	5.381	-0.495
3	2.105	14.71
4	-8.853	-22.06
5	9.122	14.44

mally cycling below M_f and above A_f at different load bias to observe the effect of load bias on each microstructure. For these experiments, the samples were first heated to the UCT of 300 °C under a low load of 10 N to fully transform the material into austenite, then loaded to a constant bias load level, P_{bias} , and thermally cycled between UCT and LCT (50 °C) at an average rate of 1.4 °C/s with a 2-min dwell time at the LCT and UCT. Additionally, at the end of every half cycle at the UCT and LCT, partial unloads and reloads were performed to measure the specimen compliance. The schematics delineated in Fig. 3a and b illustrate the different stages during an actuation cycle.

2.5. Fracture toughness analysis

The fracture toughness at each temperature and microstructure were determined by applying the modified J-integral method to the load and displacement data, as proposed in Ref. [44] and implemented in Ref. [38]. A brief description of this procedure is presented in this section. Crack mouth opening displacement (V^{CMOD}) measurements were first translated to the load line displacement (V^{LLD}) location using the following displacement translation equation (1)) developed by Newman et al. [48].

$$V^{LLD} = V^{CMOD} e^{\sum_{j=1}^{5} \left(A_{j}^{LLD} - A_{j}^{CMOD} \right) \left(\frac{a}{W} \right)^{j-1}}$$
 (1)

Before applying equation (1), V^{CMOD} measurements are used to determine the crack mouth opening compliance (C^{CMOD}) and subsequently determined the crack length, a, as per ASTM399 standard [49]. In equation (1), W represents the width of the DCT sample as defined in Ref. [48] and ASTM Standard E1820 [47]. The A_i^{CMOD} and A_i^{LLD}

coefficients consist of the values in Table 1 below, where j is the index for the summation in equation 1

For samples that exhibit fracture instability, the single-point J method was implemented as described in Ref. [44], where the J-value at the maximum load is calculated as the sum of elastic and inelastic components as shown in Eq. (2)).

$$J = J^{el} + J^{in} = \frac{\eta^{el} A^{el}}{Rh} + \frac{\eta^{in} A^{in}}{Rh}$$
 (2)

where B and b are the specimen thickness and unbroken ligament length, respectively, and A^{el} and A^{in} are the elastic and inelastic components of the area under the load-displacement curve. The elastic and inelastic geometry-dependent factors, $\eta^{el} = 1.5 + 2.02(b/W)$ and $\eta^{in} = 2.0 + 0.522(b/W)$ respectively, are also found in Ref. [44].

For the samples that exhibited stable crack growth, the R-curve method, as described in ASTM standard E1820,was used [47], where the J-value at the i^{th} unload/reload sequence is calculated as $J_i = J_i^{el} + J_i^{in}$; here, J_i^{el} and J_i^{in} are the incremental elastic and inelastic components of J_i , respectively, and are evaluated using equation (3)) and 4) below.

$$J_i^{el} = \left[J_{i-1}^{el} + \frac{\eta_{i-1}^{el}}{Bb_{i-1}} A_{i-1,i}^{el} \right] \left[1 - \frac{\gamma_{i-1}^{el}}{b_{i-1}} (a_i - a_{i-1}) \right]$$
(3)

$$J_i^{in} = \left[J_{i-1}^{in} + \frac{\eta_{i-1}^{in}}{Bb_{i-1}} A_{i-1,i}^{in} \right] \left[1 - \frac{\gamma_{i-1}^{in}}{b_{i-1}} (a_i - a_{i-1}) \right]$$
(4)

The γ_{i-1}^{el} and γ_{i-1}^{in} terms in equation (3)) and 4) above are geometry dependent factors at the i-1 unload/load iteration [44]. Similarly, b_{i-1} and η_{i-1}^{in} are the remaining ligament size and geometric factor, as defined in the fracture instability case, at the i-1 unload/load iteration. Here, the crack length, a_i , is calculated at each unload/reload sequence using the specimen load -line compliance (C_i^{LLD}), $\gamma_i^{el} = 0.5 + 2.92 (b_{i/W})$, and $\gamma_i^{in} = 1 + 0.76 (b_{i/W})$. $A_{i-1,i}^{in}$ and $A_{i-1,i}^{in}$ are the inelastic and elastic area increments between load/unload i and i-1 [44].

$$A_{i-1,i}^{el} = \frac{1}{2} (P_i + P_{i-1}) \left(V_i^{LLD,el} - V_{i-1}^{LLD,el} \right)$$
 (5)

$$A_{i-1,i}^{in} = \frac{1}{2} (P_i + P_{i-1}) \left(V_i^{LLD,in} - V_{i-1}^{LLD,in} \right)$$
 (6)

Where P_i is the maximum load just prior to unloading and the elastic and inelastic displacement are determined as $V_i^{LLD,el} = P_i C_i^{LLD}$ and $V_i^{LLD,in} = V_i^{LLD,el} - V_i^{LLD,el}$, respectively; V_i^{LLD} is the corresponding displacement at P_i . The critical J-value was then obtained from the intersection of a regression line to $J - \Delta a$ data and an offset line at 0.2 mm. More details on the aforementioned methods can be found in Refs. [38,44].

2.6. ΔJ determination in mechanical fatigue crack growth experiments

Crack growth rates were determined by constructing the modified Paris-Erdogan curve, $\frac{da}{dN}vs\Delta J$. The three regimes observed include the threshold regime, the steady crack growth regime, and the unstable crack growth regime, where the steady crack growth regime is linear and can be fitted by a power-law equation commonly referred to as Paris equation.

$$\frac{da}{dN} = C\Delta J^m \tag{7}$$

where $\frac{da}{dN}$ is the fatigue crack growth for the load cycle N, ΔJ is the strain energy release rate range. C and m are experimentally obtained material coefficients. The experimental measurement of ΔJ in the presence of large hysteresis in the load displacement responses can be determined as described in Ref. [41] with the following equation

$$\Delta J = \Delta J^{el} + \Delta J^{in} = \frac{\eta^{el} \Delta A^{el}}{Rb} + \frac{\eta^{in} \Delta A^{in}}{Rb}$$
(8)

where ΔA^{in} corresponds to the area of the hysteresis loop between the loading and unloading curves of the ΔP vs. ΔV^{LLD} response and ΔA^{el} is the total area under the loading ΔP vs. ΔV^{LLD} curve minus the hysteresis loop area. These areas can be approximated by determining the displacements corresponding to the elastic $(\Delta V^{LLD,el})$ and inelastic $(\Delta V^{LLD,in})$ areas. Here, $\Delta V^{LLD,el}$ can be determined using the compliance during unloading $(C^{LLD,unloading})$ before unloading deviates from linearity using equation 9) as schematically illustrated in Ref. [41].

$$\Delta V^{LLD,el} = C^{LLD,unloading}(P_{max} - P_{min}) = C^{LLD,unloading}(\Delta P)$$
(9)

and

$$\Delta V^{LLD,in} = \Delta V^{LLD} - \Delta V^{LLD,el} \tag{10}$$

ther

$$\Delta A^{el} = \frac{1}{2} (P_{max} - P_{min}) \Delta V^{LLD,el} = \frac{1}{2} (\Delta P) \Delta V^{LLD,el}$$
(11)

and

$$\Delta A^{in} = \int_{V_{min}}^{V_{max}^{LLD}} (P - P_{min}) dV - \Delta A^{el}$$
(12)

Finally, crack growth rates, $\frac{da}{dv}$ are calculated taking the slope between two subsequent points on the $\Delta a vs N$ curves, using the procedure described in ASTM E647 [50].

2.7. ΔJ determination in actuation fatigue crack growth experiments

In actuation crack growth, specimens are thermally cycled between an LCT below M_s and a UCT above A_f under a constant load bias; this is schematically shown in Fig. 3. Equation 8) is also employed during actuation crack growth to determine ΔJ . However, the ΔA^{el} and ΔA^{in} areas are determined by the phase change driven displacement, ΔV^{LLD} , at the contact load P_{bias} . The total displacement ΔV^{LLD} is the difference between $V^{LLD}_{max} - V^{LLD}_{min}$, corresponding to stage (2) for V^{LLD}_{max} and stage (1) for V^{LLD}_{min} in Fig. 3a. The elastic displacement component, $\Delta V^{LLD,el}$, accompanying this displacement is associated to the recoverable displacement in the austenite phase, and is calculated using the compliance in the austenite phase, C^{LLD}_{cl} , attained during partial unloading in stages (2-3-4) in Fig. 3a. A schematic illustration of these areas are also shown in Ref. [41]. The elastic displacement can be calculated as

$$\Delta V^{LLD,el} = C_{Aus}^{LLD} P_{bias}$$

Then ΔA^{el} is

$$\Delta A^{el} = \frac{1}{2} \Delta V^{LLD,el} P_{bias}$$

Finally, ΔA^{in} can be determined as

$$\Delta A^{in} = P_{bias} \Delta V^{LLD} - \Delta A^{el}$$

The compliance in the martensite phase, C_{Mar}^{LLD} , was also determined by partially unloading at stages (5-6-7) in Fig. 3a. This is done to compute the martensite phase crack extension since $\frac{da}{dN}$ has been observed during forward transformation in previous actuation experiments [41,51]. Moreover, visual crack measurements are not easily attainable in the austenite phase due to crack closure. We direct readers interested on a more detailed description of the mechanical and actuation fatigue crack growth ΔJ determination procedures to Ref. [41].

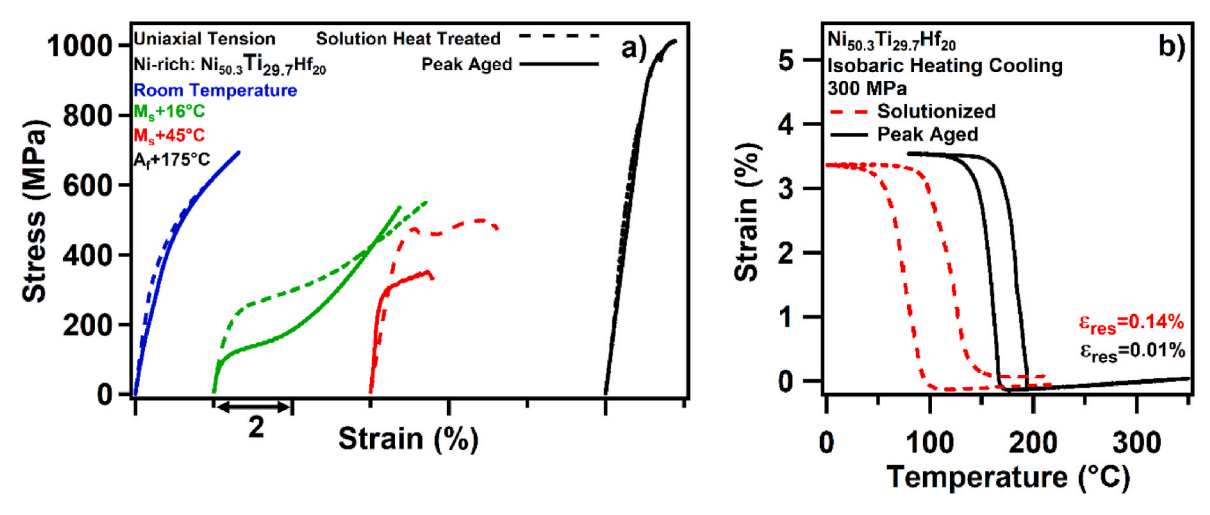


Fig. 4. (a) Uniaxial tensile experiments for PA (solid line) and SHT conditions (dashed line) from left to right: Room temperature (blue), M_s +15 °C (Green), M_s +45 °C (red), and A_f +175 °C (black). (b) Isobaric heating cooling tensile experiments for SHT (left) and PA (right) conditions at 300 MPa. Note the significant difference in residual strain ($ε_{res}$) between the PA and SHT conditions in a single thermal cycle. (For interpretation of the references to colour in this figure legend, the reader is referred to the Web version of this article.)

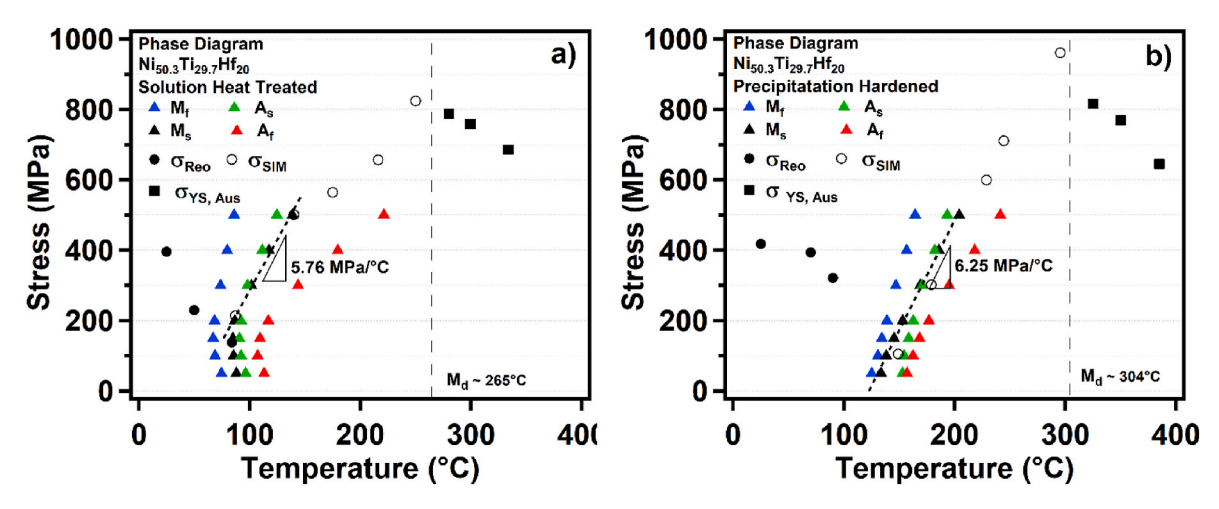


Fig. 5. Stress vs. temperature phase diagrams for Ni_{50.3}Ti_{29.7}Hf₂₀ HTSMA in (a) solution heat treated (900 °C for 1 h) condition with a Clausius-Clapeyron slope of 5.76 MPA/°C and (b) peak aged (550 °C for 3 h) condition with a Clausius-Clapeyron slope of 6.25 MPA/°C.

3. Results and discussion

3.1. Uniaxial tension experiments

A combination of isobaric and isothermal experiments (Fig. 4) was used to construct the stress-temperature phase diagrams, seen in Fig. 5 for the SHT and PA conditions. The selected uniaxial tension results presented in Fig. 4a correspond to temperatures close to those used for the fracture toughness experiments. Starkly different mechanical behaviors are seen among the different test temperatures presented. Characterizing the deformation during uniaxial loading helps expand understanding of material behavior during fracture toughness tests and will be discussed more with the fracture toughness results (Section 3.2). For the two experiments at room temperature (below M_f), the initial microstructure of self-accommodated martensite deforms elastically before undergoing martensite detwinning/reorientation. Thus, the samples most likely fail before the detwinning is completed in both cases due to the low strain levels recorded at the failure. The stresses required to detwin the PA and SHT microstructures at room-temperature are similar, but the SHT condition has a lower failure strength and lower total elongation than that of the PA condition.

The testing temperature for uniaxial tension experiments that

martensitically transform under stress were normalized with respect to their M_s , as M_s +45 °C, to compare the thermomechanical response of each material condition at an equal temperature difference from their M_s temperature. These temperatures correspond to 114 °C and 179 °C in SHT and PA conditions, respectively. In the presence of martensitic transformation, SHT NiTiHf exhibits a significantly higher elongation and failure strength. Both microstructures exhibit high strain-hardening coefficients (11.5 \pm 1 GPa), indicating the difficulty of detwinning martensite in NiTiHf as previously reported in the literature [38,52,53]. Moreover, three distinct stages of loading can be observed at M_s +45 °C. First, the samples elastically deform in austenite. Then, they undergo SIM transformation, which leads to a "plateau" region of lower slope than the previous elastic loading. Finally, the stress induced martensite deforms elastically in the third stage of loading, resulting in a third distinct slope. When compared to the martensitic material, the samples that undergo SIM transformation have significantly higher elongation. This indicates that phase transformation causes the material to have higher ductility than martensite detwinning.

Fig. 4a also shows the monotonic test results for samples that remain in the austenitic phase during the entire test. The test temperatures of these samples were normalized with respect to their A_f temperatures, as $A_f + 175$ °C, to observe the thermomechanical response of each material

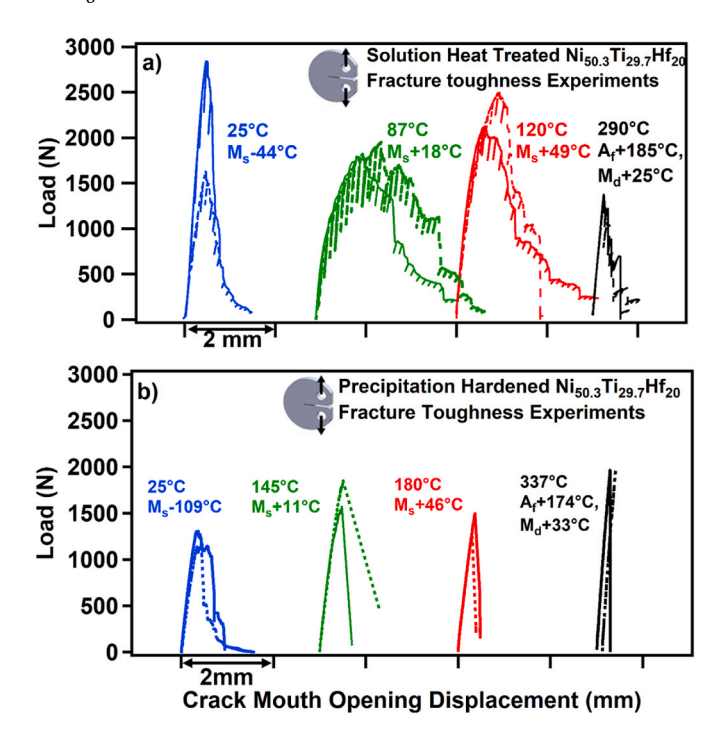


Fig. 6. Load (N) vs. Crack Mouth Opening Displacement (CMOD) curves of the $Ni_{50.3}Ti_{29.7}Hf_{20}$ HTSMA for the SHT **(a)** and PA **(b)** conditions. Test temperatures were selected such that fully martensitic (blue), martensitically transforming austenite (green and red), and fully austenite (black) phases were tested. (For interpretation of the references to colour in this figure legend, the reader is referred to the Web version of this article.)

condition at a temperature close to the fully austenite fracture toughness test presented in the following section. These temperatures correspond to 280 °C (the martensite desist (M_d) temperature + 15 °C) and 338 °C (M_d + 34 °C) for SHT and PA conditions, respectively. In these experiments, the austenite phase exhibits elastic behavior until it reaches a yield point, after which it exhibits plastic behavior. This is expected due to this test temperature being above the M_d temperature (the temperature above which the stress required to plastically deform austenite is lower than the stress required to trigger stress-induced martensite). In the IHC actuation cycle at 300 MPa, Fig. 4b, the SHT condition shows significantly more residual strain, 0.14%, than the PA condition, 0.01%, after a thermal cycle. This is the result of nano-precipitates in the PA microstructure pinning dislocations (which accompany phase transformation) and preventing their movement, which does not occur in the SHT microstructure due to lack of precipitates.

Additional IHC curves were generated at loads of 50, 100, 150, 200, 300, 400, and 500 MPa, not shown, were used to construct the phase diagrams for the SHT (Fig. 5a) and PA (Fig. 5b) material conditions. Clausius-Clapeyron slopes of 5.76 MPA/°C and 6.25 MPA/°C for SHT and PA, respectively, were determined. The higher slope of the nanoprecipitation hardened NiTiHf agrees with the higher load required to reach SIM in PA condition at M_s +45 °C compared to SHT during monotonic tension (Fig. 4a). Moreover, SIM values above 500 MPa attained during monotonic tension align better with the Clausius-Clapeyron slope in precipitation-hardened material (Fig. 5b) compared to the precipitate-free one (Fig. 5a). This can be attributed to lower resistance to dislocation accumulations (i.e., plasticity) in the SHT austenite phase, leading to easier dislocation formation and accumulation under high stress levels. As a result of these dislocations, a higher strain field is formed, leading to premature SIM induced by the larger strain field [54].

Finally, Fig. 5 is also used to determine the M_d values. The interception of the best fit curves in Fig. 5 in the region that is mainly governed by SIM and the region where the yield strength is dictated mainly

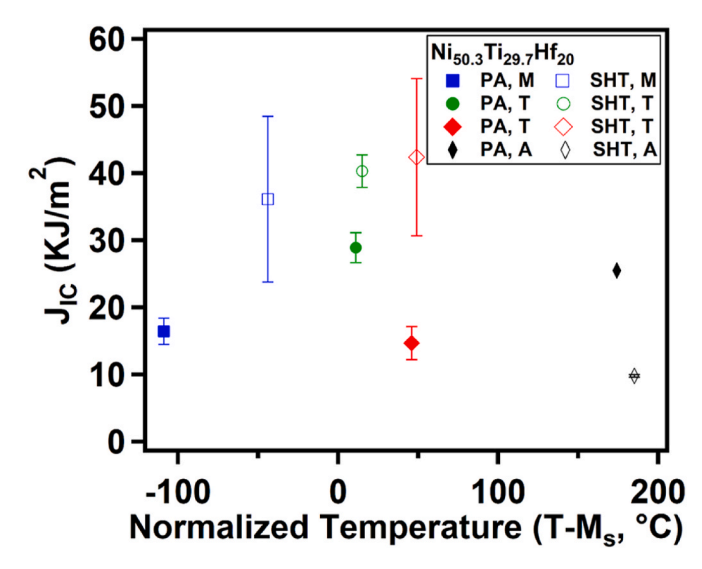


Fig. 7. Average fracture toughness (J_{IC}) values for PA (solid markers) and SHT (open markers) conditions plotted against normalized temperature $(T - M_s)$. M: Martensite, T: Martensitically Transforming austenite, A: Austenite.

by the plastic deformation of the austenite results in the M_d values as $\sim\!265\,^\circ\text{C}$ in SHT condition and $\sim\!304\,^\circ\text{C}$ in PA condition.

3.2. Fracture toughness experiments

Load-CMOD curves obtained from the DCT specimens are presented in Fig. 6. The DCT specimens were tested at temperatures similar to the ones used for the uniaxial tension experiments presented in Fig. 4a. The initial crack lengths of all the specimens were $a_0=10\pm 1$ mm, and the periodic load drops on the load-displacement curves are a result of unloading-reloading sequences performed throughout the test to capture specimen compliance and construct resistance curves (R-curves) when steady crack growth was observed [44,47]. Fracture toughness tests were performed on fully martensitic state, fully austenitic state, and across martensitic transformation. At room temperature, i.e., fully martensitic case, the SHT condition reached a higher maximum load, compared to PA condition, before failure. Both SHT and PA specimen conditions exhibited brittle fracture. However, PA NiTiHf demonstrated more consistent maximum load values between different experiments compared to the SHT condition. Next, two fracture toughness experiments were performed across martensitic transformation. In PA NiTiHf, both tests, at M_s +11 °C and M_s +46 °C, exhibited brittle fracture. SHT NiTiHf, on the other hand, exhibited significant resistance to crack growth for both tests, M_s +18 °C and M_s +49 °C, across martensitic transformation. Finally, fracture toughness experiments in SHT and PA NiTiHf were also performed at fully austenitic states. Both cases exhibited low fracture toughness values. This is a result of the limited plasticity of austenitic NiTiHf, as revealed by monotonic tension experiments in Fig. 4a, that led to low crack tip stress relaxation. The fracture toughness, J_{IC} , of austenite in the PA material is higher than that of the SHT material. This is attributed to the ductility-strength trade off due to precipitation hardening.

In Fig. 7, the critical J-values, J_{IC} , for unstable crack growth are compiled. It can be seen in the figure that there is a noticeable increase in J_{IC} in the SHT and PA NiTiHf cases across martensitic transformation (at 0 °C< $T-M_s$ < 100 °C). The larger inelasticity observed in SHT NiTiHf during monotonic tension experiments across martensitic transformation (Fig. 4a) correlates well with larger CMOD values attained during fracture toughness testing (Fig. 6). This is a result of the stress relaxation at the crack tip and accompanying martensitic transformation. Although enhancement in inelasticity was also observed in PA NiTiHf during monotonic tension across martensitic transformation,

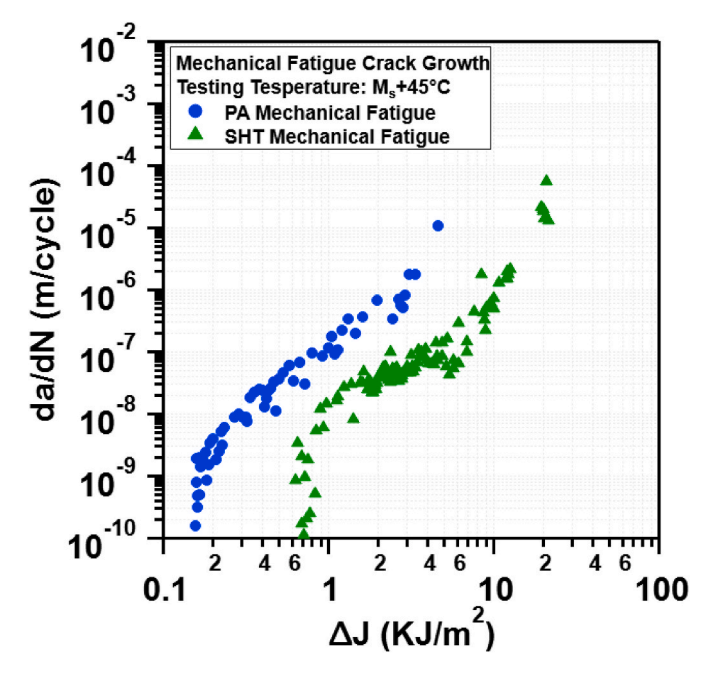


Fig. 8. $\Delta J w \frac{da}{dN}$ plot for mechanical fatigue crack growth response of the Ni_{50.3}Ti_{29.7}Hf₂₀ DCT specimens at M_s +45 °C (in austenite). The PA condition has a lower threshold, ΔJ , and a higher Paris exponent, m, than the SHT material.

limited CMOD was observed for this condition during fracture toughness testing. There are two possible mechanisms playing a role in this microstructure. 1) dislocations emanating from the martensite [55] at the crack tip are not able to glide into the surrounding austenite, nor

sufficiently relax stress at the crack tip, due to H-phase precipitates pinning down the glide of such dislocations. 2) The strain localization at the crack tip increases stresses at the H-precipitates interfaces [56] leading to their failure, which in turn coalesce to form cracks of critical size leading to unstable crack growth. Fig. 6 shows that the austenitic NiTiHf exhibits brittle failure regardless of the presence of precipitates. Instead, the brittle fracture of austenite occurs due to its low ductility (Fig. 4a) leading to low crack tip stress relaxation. Thus, it can be concluded that the toughness enhancement in SHT NiTiHf is mainly a result of martensitic transformation and case 1) above can be ruled out. Thus, because the load-CMOD plots for PA NiTiHf at M_s +11 °C and M_s +46 °C are linear before reaching a maximum load, it can be speculated that the specimens fail by mechanism 2) before significant martensitic transformation could take place. Hence, it can be concluded that although precipitates play an important role in stabilizing the functional fatigue performance of NiTiHf, they lower the ability of NiTiHf to resist crack nucleation and unstable crack growth.

3.3. Fatigue crack growth experiments

3.3.1. Mechanical fatigue crack growth

Mechanical fatigue crack growth experiments were performed to construct the Paris Law plot (Fig. 8). It should be noted that since there is no appreciable inelastic deformation near the crack tip, especially in the PA case, the driving force for these experiments could feasibly be described as ΔK , but ΔJ is used instead to be able to compare the results with those from the actuation fatigue crack growth experiments. From the plot, several conclusions can be drawn about the differences in the crack growth behavior between the PA and SHT conditions. The threshold (ΔJ_{th}) is ~ 0.14 kJ/m² in the PA condition, and ~ 0.7 kJ/m² in the SHT condition. These thresholds are obtained from the operational definition of when the crack growth rate reaches 10^{-10} m/cycle [50].

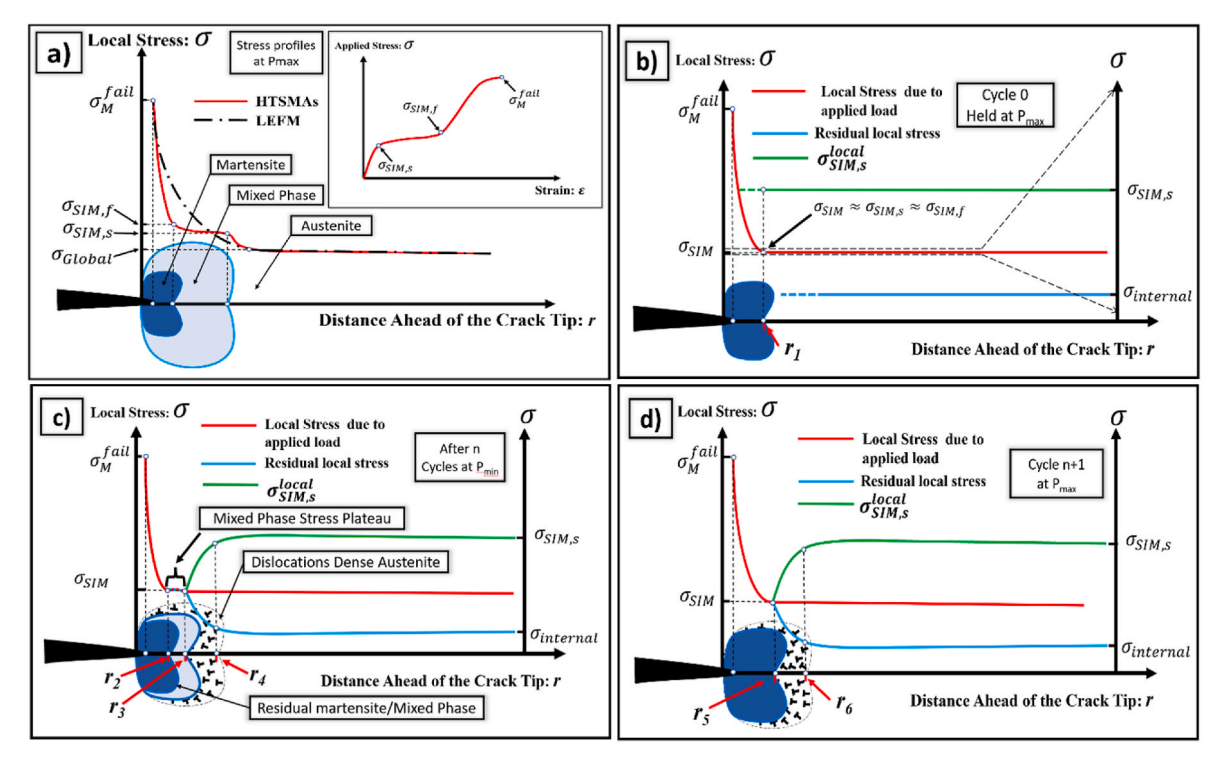


Fig. 9. Mechanisms involved during stable mechanical crack growth in precipitate-free (i.e., SHT) NiTiHf with schematic a) first illustrating the stress profiles for conventional alloys vs. SMAs/HTSMA when held at P_{max} . b) Stress profile for a given SMAs/HTSMA held at P_{max} in the vicinity of an existing defect/crack prior to mechanical cycling. The second axis is added to illustrate the effect of cycling on the evolution of the internal stresses and the stress required to begin forward transformation ($\sigma_{sim,s}$) as defined by the inset in a). c) Stress profile around the crack after a given number n of cycles with the appearance of a dislocation dense austenite region and a mixed phase region. d) stress and microstructure profile at n+1 cycle at P_{max} illustrating the introduction of a larger dislocation dense zone in austenite and fully transformed mixed mode phase into martensite phase.

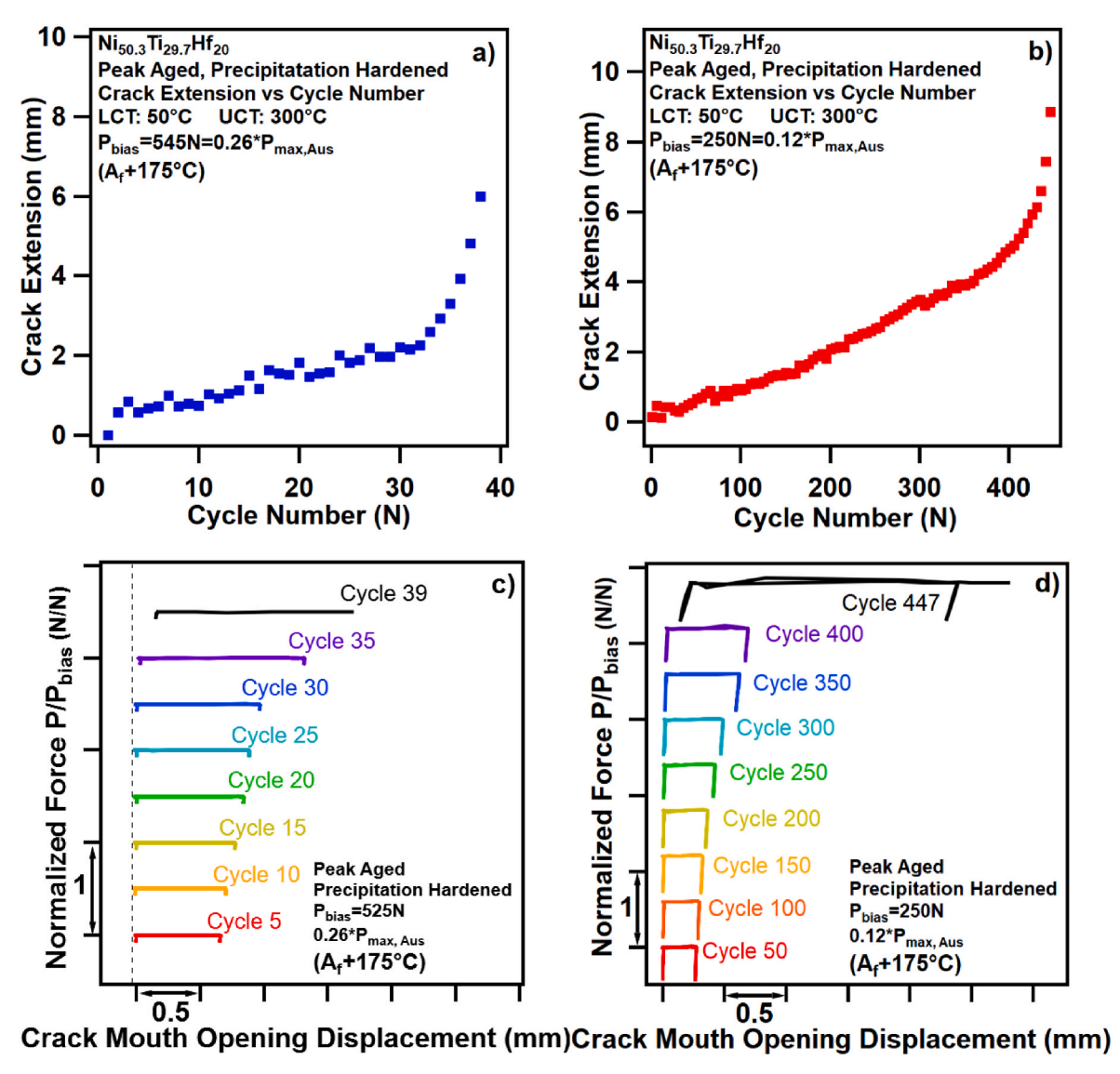


Fig. 10. Crack extension vs. cycle number plots of the peak aged $Ni_{50.3}Ti_{29.7}Hf_{20}$ HTSMA of martensite phase under bias loads (a) $P_{bias} = 525$ N, which lasted for 38 complete actuation cycles and failed on the 39th during cooling and (b) $P_{bias} = 250$ N, which lasted for 448 complete actuation cycles and failed on the 449th.

The steady-state region of crack growth has been fitted with the modified Paris Law, eq. 7). The C and m coefficients were measured to be $C_{PA} = 12 \times 10^{-8}$ (m/cycle)/(kJ/m²)^m, $m_{PA} = 2.2$, $C_{SHT} = 1.4 \times 10^{-8}$ (m/cycle)/(kJ/m²)^m, and $m_{SHT} = 1.1$. From the Paris Law plots and the fitted constants of the mechanical fatigue crack growth experiments, it is seen that the SHT condition has a lower slope for the steady crack growth region.

To reason through a plausible scenario leading to the lower slope in SHT NiTiHf, Fig. 9 presents a series of schematics elucidating the possible mechanisms involved during mechanical fatigue crack growth experiments in SHT NiTiHf. Fig. 9a first shows a schematic comparing the local stress profile at a crack tip for a traditional non transforming alloy (LEFM line) and a HTSMA in the superelastic temperature range in the presence of a defect (i.e., crack) while held at the Pmax load. There, it can clearly be seen that the HTSMA, unlike traditional nontransforming alloys, may contain a mix phase region, composed of austenite and retained martensite, at the maximum load, which relieves some of the stress generated by the stress intensity field around the crack tip. The inset in Fig. 9a presents a monotonic tension test schematic for a HTSMA undergoing SIM with $\sigma_{SIM.s}$ and $\sigma_{SIM.f}$ defined as the start and finish points of martensitic transformation.

The conditions in which the mixed phase region may develop in a

given SMA/HTSMA, and can significantly influence the crack growth rate, will be discussed sequentially with the help of Fig. 9b thought 9d. The insert in Fig. 9a shows that the stress range between $\sigma_{SIM.s}$ and $\sigma_{SIM.f}$ is relatively small compared to elastic regions of the austenite and martensite phases. Thus, due to the small stress range of this plateau and the exponential stress increase as the crack tip is approached, Fig. 9b introduces a new schematic for a precipitate-free HTSMA prior to mechanical cycling and held at P_{max} , in which $\sigma_{SIM,s}$ and $\sigma_{SIM,f}$ are all approximated on the left Y-axis as a single value, σ_{SIM} . This approximation is supported by the in-situ synchrotron low -cycle mechanical fatigue experiments performed by Robertson et al. in Ref. [57] where the mixed phase region was only stable in a negligible region around the martensite zone at the crack tip. The Y-axis on the right-hand side of the schematic is an exploded view of the stress in the vicinity of σ_{SIM} . This axis will be used to elucidate how the $\sigma_{SIM,s}$, as defined by the inset in Fig. 9a, is affected by mechanical cycling in the presence of a crack. Moreover, an arbitrary value, $\sigma_{internal}$, is also assigned to the internal stress in the austenite phase in HTSMAs on the right Y-axis to illustrate the role of residual stresses evolution during mechanical cycling.

Fig. 9c proposes a crack tip stress profile, with martensite size $r_2 > r_1$, after being subjected to n number of cycles and held at P_{min} . This region primarily consists of retained martensite and heavy dislocation

density. Then the next region $(r_2 < r < r_3)$ is the mixed phase region which composes of dislocations, retained martensite and austenite and evolves as a result of the compounding stresses applied during mechanical cycling, the stress intensity raiser, i.e., crack, and residual stresses due to dislocation networks and oriented martensite boundaries. Note that dislocations in these regions $(r < r_3)$ are not shown in the schematics for the sake of clarity. The next region $(r_3 < r < r_4)$ is the austenite region with dislocations which form due to cyclic phase transformation and transformation induced plasticity. These dislocations in the austenite phase play a dual role. 1) They assist in the formation of martensite by locally lowering the $\sigma_{SIM.s}$ value in the following cycles) [54], and 2) increase the internal stresses in the austenite phase. Such internal stresses eventually reach the lowered local $\sigma_{SIM.s}$ value as they crack tip is approached, at which point martensite is retained (location r_3). It is speculated that the combination of the lowering $\sigma_{SIM.s.}$ and increasing residual local stresses enable the appearance of a non-negligible mix phase region which accumulates with repeated cycling. This is shown Fig. 9c by a narrow stress plateau region between locations r_2 and r_3 . In the subsequent cycles, the mixed phase region contributes to the stress relaxation at the crack tip with the energy dissipation required to fully transform the mixed phase at the crack tip.

Next, a snapshot of the crack tip stress profile at $P_{\rm max}$ during cycle n+1 is presented in Fig. 9d. The increased applied load drives the martensite zone to grow slightly larger than the mixed phase region at cycle n ($r_5 > r_3$). Such larger martensite zone will in turn increase the dislocation density in the austenite ($r_6 > r_4$) as well as the mixed phase zone when the load is reduced back to $P_{\rm min}$ during the n+1 cycle. This mechanism is an iterative process in which the energy dissipation capability of the material (i.e., mixed phase zone) seems to grow with increasing cycling while the region with a lowered $\sigma_{SIM,s}$ value grows (i. e., dislocation dense austenite) until a steady state is reached. At this point, the steady crack growth regime in the Paris-Erdogan plot has been reached, which in the case of SHT NiTiHf is with a lower slope due to the energy dissipative mechanism provided by the relatively large mixed phase zone having considerable dislocation density ahead of the crack tip.

On the other hand, the nanoprecipitates present in PA NiTiHf do not allow high dislocation density in the austenite region [58] around the crack tip as compared to the SHT NiTiHf case. Thus, although a similar steady state energy dissipative capability may exist, this is probably limited to a much narrower stress plateau ahead of the crack tip due to the limited formation of mixed phase region ahead of the crack tip. Nonetheless, this more direct martensite-to-austenite phase change and lack of dislocations in PA NiTiHf also stabilizes functional fatigue. Unfortunately, TEM evidence of the proposed mechanisms, although attempted, could not be achieved due to the loss of boundary conditions after using focused ion beam (FIB) micromachining in the vicinity of the crack tip. Hence, in-situ structural fatigue must be performed to corroborate the proposed mechanism here.

3.3.2. Actuation fatigue crack growth

For the PA condition, stable crack growth is observed for the tested bias loads, $P_{\text{bias}} = 525 \text{ N}$ and 250 N (26% and 12% of P_{PA}^{MAX} at $A_f + 175 \,^{\circ}\text{C}$, respectively). In Fig. 10a, a bias load of 525 N results in 38 complete actuation cycles, and failure during cooling on the 39th cycle. In Fig. 10b–a bias load of 250 N results in 448 complete actuation cycles, and failure during cooling on the 449th (every fiftieth cycle is shown for clarity). The corresponding normalized load vs. CMOD plots for the PA condition can be seen in Fig. 10c and d for the two loads, respectively.

These results are somewhat similar to the actuation fatigue crack growth experiments in NiTi SMAs where the crack is observed to grow during the cooling portion of the temperature cycle [41,59,60]. Additionally, crack growth during cooling is mostly linear with respect to cycle number throughout most of the tests (Fig. 10a and 10b), with the instability occurring at the very end, and accounting for about half or

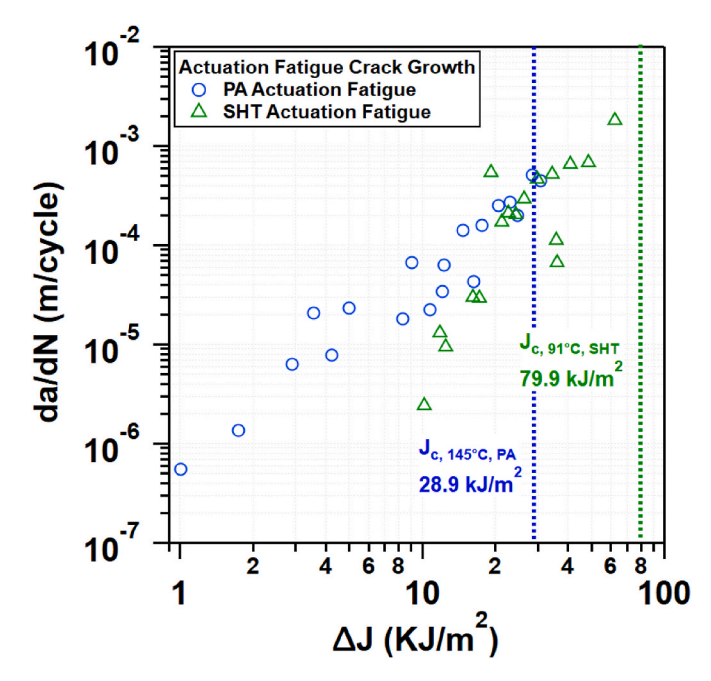


Fig. 11. da/dN vs. ΔJ plots for the actuation fatigue crack growth of the Ni_{50.3}Ti_{29.7}Hf₂₀ DCT specimens. The PA condition has a lower fracture toughness than the SHT material, which explains the difference between the regime-3 portions of the Paris Law curve and unstable crack growth regime.

more of the total crack extension. Much like the crack length, the change in CMOD per cycle (Δ CMOD) during cooling increases steadily throughout the experiment, and as the samples approach final failure, increases very rapidly. On the other hand, crack growth during heating remains stagnant for the majority of the experiment, but it can be seen that as the specimen approaches final failure, the CMOD at high temperatures also increases (i.e., apparent crack closure decreases, Fig. 10c).

These fatigue crack growth experiments can be used to construct part of a Paris Law curve and unstable crack growth regime, in which a driving force, ΔJ , is plotted against a fatigue crack growth rate $\frac{da}{dN}$ on a log-log plot, as shown in Fig. 11. A detailed explanation on how to calculate the driving force can be found in Ref. [41]. The Paris Law curve is further discussed at the end of the section.

For the SHT condition, bias loads that are over 50% of the maximum load of the $A_f+175\,^{\circ}\mathrm{C}$ fracture toughness experiments resulted in fast crack growth over a small number of cycles. In Fig. 12a, a bias load of 1200 N on SHT specimens resulted in only two complete actuation cycles, and failure during cooling on the third cycle, while a bias load of 900 N (Fig. 12b) resulted in 9 complete actuation cycles and failure during heating on the 10th. A comparison of the CMOD vs. normalized load for both $P_{\text{bias}}=1200$ N and 900 N (80% and 60% of P_{SHT}^{MAX} at $A_f+175\,^{\circ}\mathrm{C}$, respectively) can be found in Fig. 12c and 12d. In Fig. 11, the driving force, ΔJ_i is plotted against the fatigue crack growth rate $\frac{da}{dN}$ for the SHT condition as well.

In the experiment performed at a lower P_{bias} in the SHT condition, no steady crack growth was observed for hundreds of actuation cycles although tested at a higher relative bias load than the PA material. In order to take a closer look at this phenomenon, the normalized load vs. CMOD plots for two actuation fatigue crack growth experiments, one in the PA condition, $P_{bias}=250\ N$, and the other in the SHT condition $P_{bias}=350\ N$, where the PA condition is tested at a lower relative load than the SHT condition, are shown in Fig. 13. Under a bias load of 350 N, the first 10 cycles in the SHT condition appear to follow a trend like the PA material. However, between 10 and 20 cycles, the amount that the Δ CMOD grows is less than the initial 10 cycles. After cycle 20, the Δ

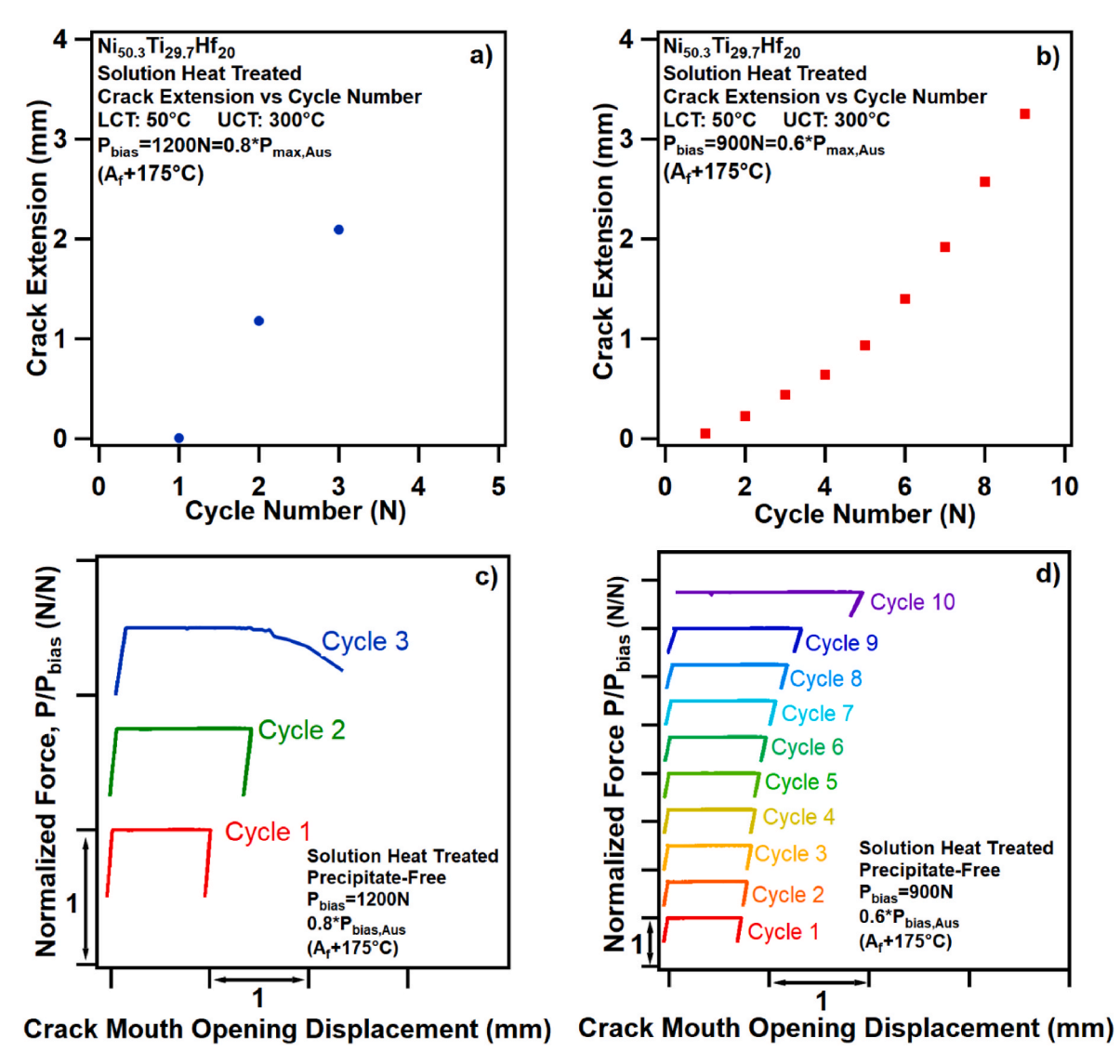


Fig. 12. Crack extension vs. cycle number plots of the $Ni_{50.3}Ti_{29.7}Hf_{20}$ HTSMA in solution heat treated condition at bias loads (a) $P_{bias} = 1200$ N, which lasted for 2 complete actuation cycles and failed on the 3rd cycle during cooling and (b) $P_{bias} = 900$ N, which lasted for 9 complete actuation cycles and failed on the 10th during heating. (c) (d) CMOD vs. normalized force plots are also shown for the two conditions corresponding to (a) and (b).

CMOD decreases until it reaches an approximate asymptote in cycle 350. After cycle 439, the test was interrupted, because no crack growth was seen.

During the actuation fatigue crack growth experiments, the samples undergo martensitic transformation in the entire sample in each cycle and it is apparent, from the isobaric heating cooling strain-temperature curves (Fig. 4b), that the amount of irrecoverable strain is significantly higher in the SHT condition when compared to the PA condition. This residual strain in the SHT condition is a combination of plasticity and retained martensite, which exists because dislocation networks forming during repeated transformation do not allow the martensite to transform back into austenite. To illustrate this better, the schematic in Fig. 14a shows a dislocations zone in front of the crack tip engulfing retained martensite near the crack tip at the upper cycle temperature (UCT). The sizes of the retained martensite, mixed phase, and dislocations dense austenite regions, r_m , r_i , r_d , respectively, after a given n number of actuation cycles is also shown Fig. 14a. In the subsequent cycles n₁and n_2 , where $n_2 > n_1 > n$, the mixed mode region increases due to transformation induced plasticity and conventional plasticity during the actuation cycling [61], thus increasing the energy dissipation. Moreover, during actuation, the entire sample undergoes martensitic transformation. Thus, transformation induced plasticity introduce, not only residual stresses in the vicinity of the crack tip, but also in the entire sample. This is illustrated in Fig. 14a where the residual (internal) local stress plateau is increasing with increasing actuation cycling. The grayed out dashed lines shown in Fig. 14a are repurposed to show not only future austenite dense locations at n_1 and n_2 number of cycles, but also future mixed phase regions. Note that the size of retained martensite region after n_1 and n_2 number of cycles is not shown because its size is highly depended on the bias load.

Based on the schematic in Fig. 14a–if the size of the fully martensite region (r_m) does not increase at equal or higher rate than the growth rate of the mixed mode/retained martensite region (r_i) , crack arrest will take place. This is the case because, during actuation, the size of the martensite region is dependent on the bias load and crack size (i.e., driving force). The mixed mode region, on the other hand, not only depends on the applied load and crack size, but also on residual stresses induced during actuation cycles. Thus, actuation cycling will increase the amount of dislocations dense austenite, and as a result increase the mixed mode/retained martensite region (where the reverse transformation can still readily occur), while the ability of the near complete retained martensite zone to grow is limited by the constant bias load. In

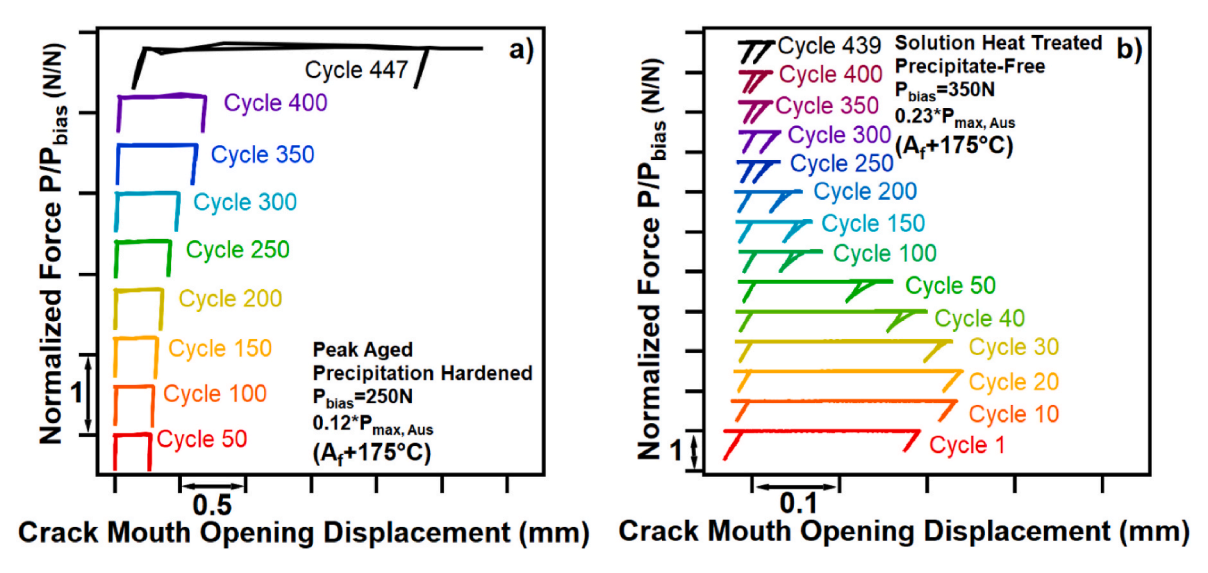


Fig. 13. Normalized load vs. CMOD for the PA condition, $P_{bias} = 250$ N (a) and the precipitate-free SHT condition, $P_{bias} = 350$ N (b). In the PA condition, Δ CMOD increases steadily over the lifetime, reaching final instability as it fails in cycle 447. In the SHT condition, Δ CMOD initially increases, but then stalls and decreases asymptotically. Note the differences in the x-axis scale (almost an order of magnitude difference) and the difference in P_{bias} . P_{bias} for the PA case is only 12% of the maximum load reached in Austenite, compared to the 23% in the SHT case.

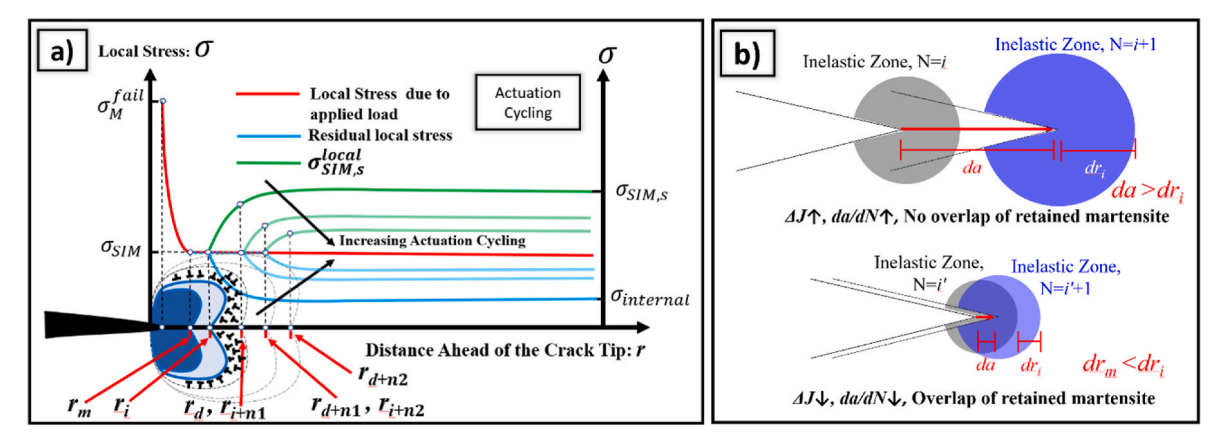


Fig. 14. a) Evolution of microstructure and stress profile of a HTSMA due to actuation cycling. r_m , r_i , and r_d represent the martensite, mixed phases, and dislocation dense zones, respectively, after an n given number cycles. Increasing mixed phase and dislocation dense profiles are presented after a given n_1 and n_2 number of cycles ($n_1 < n_2$) while the martensite zone stays relatively unchanged due to insufficient driving force. b) Schematic representation of influence of bias load on crack growth rate stability.

short, the only way to overcome the mixed-phase plateau (i.e, dissipative energy capability) is by increasing the bias load.

The schematic presented in Fig. 14b illustrates two scenarios. In the upper figure, a sufficiently large load bias is applied such that the crack growth is capable of growing pass the retained martensite region. The lower half illustrates an overlap of retained martensite zones which continuously increases and cannot be overcome by the crack due to the insufficiently large bias load. Such a mechanism would explain why the bias load is crucial during actuation crack growth in SHT NiTiHf. This mechanistic hypothesis also aids in understanding the results shown in Fig. 13b. There, the driving force of the crack is initially higher than the dissipative energy capability of the material. However, continued cycling widens the stress plateau while the crack's driving force is limited by the constant bias load, thus the crack length stops increasing.

In order to investigate this further, the sample that had previously been cycled at 350 N for $\sim\!450$ cycles (Fig. 13) was heated to and held at 350 °C for 10 min, and cooled down to room temperature under small load (10 N). This was done to remove the residual martensite that had built up at the crack tip, by overheating the sample. Even so, when significantly greater load of 1400 N is applied to the sample during

actuation cycling, Δ CMOD still decreases before the sample displays steady crack growth (Fig. 15a). This is even more evident when compared to Fig. 15b, which uses a sample that had not been previously cycled at a lower P_{bias} , showing fewer cycles to failure. This demonstrates that the dislocation network forming due to transformation cycling is quite effective to slow down the crack growth even at high bias loads as compared to the virgin samples.

Most of the displacement change, and thus the driving force, of the actuation fatigue crack growth experiments originates from the martensitic transformation. Therefore, when a large amount of retained martensite exists at the crack tip during actuation cycling, less material can transform, resulting in less transformation strain (and less displacement change). The driving force then decreases accordingly. In contrast, the driving force of mechanical fatigue crack growth relies on change in force with a constant P_{max} to create a displacement change. Whether the initial microstructure of the HTSMA at the crack tip is martensite or austenite, the load will be continually applied until the P_{max} load is reached. This means, mechanical loading is agnostic to the microstructure and will generate any required amount of displacement to achieve the target P_{max} regardless of the existence of retained

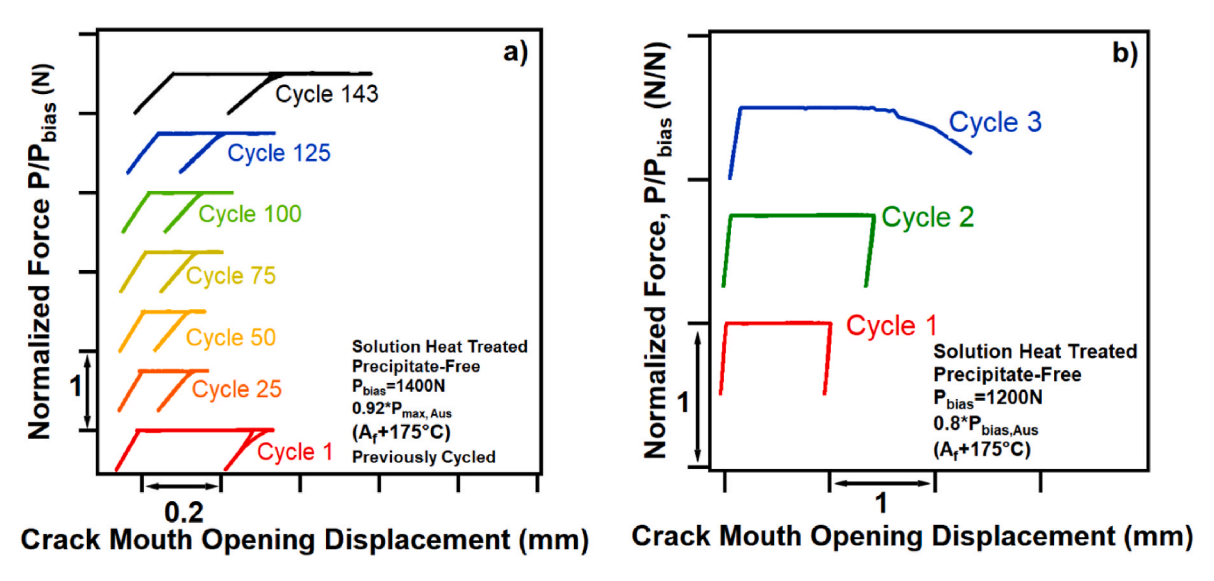


Fig. 15. Normalized load vs. CMOD graphs for **(a)** an SHT sample that had previously been cycled ~450 times at 350 N, then heated to 350 °C to remove residual martensite, then cycled at 1400 N. The effect of previous cycling still slows down the crack growth significantly and the previous thermomechanical history influences the fatigue crack growth behavior of the SHT condition. **(b)** Another SHT sample that was not previously cycled and with a lower P_{bias} than **(a)**, but failing under significantly less number of cycles, and no decrease in Δ CMOD.

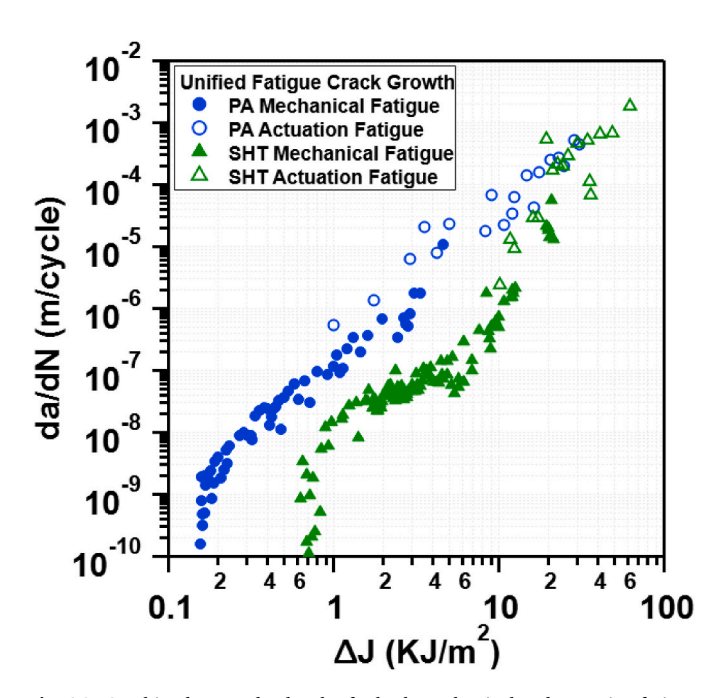


Fig. 16. Combined ΔJ vs. da/dN plot for both mechanical and actuation fatigue crack growth responses of the Ni $_{50.3}$ Ti $_{29.7}$ Hf $_{20}$ DCT specimens. The PA condition demonstrates that a unified description for the thermomechanical fatigue crack growth response of HTSMAs is possible.

martensite and dislocation structures at the crack tip. Therefore, we do not see a decrease in driving force in mechanical fatigue crack growth in the same way that we do for actuation fatigue crack growth in the SHT condition.

 $\frac{d\alpha}{dN}-\Delta J$ plots obtained from the mechanical fatigue tests performed in PA and SHT as well as the results obtained from the actuation fatigue tests in PA condition were used to construct full Paris Equation curves, seen in Fig. 16. Both microstructures exhibit the typical threshold, stable crack growth, and unstable crack growth regimes with a final failure envelope constructed using the fracture toughness values. Most importantly, it appears that the Paris Equation from mechanical fatigue crack growth experiments can be used to predict the actuation fatigue crack

growth rates for the precipitation-hardened material. On the other hand, due to the low number of cycles before unstable crack growth during actuation fatigue crack in precipitate-free material, the obtained $\frac{da}{dN} vs\Delta J$ values for this material did not align within the steady crack growth regime where the Paris equation can be fit. Therefore, the ability to predict steady actuation crack growth rates in precipitate-free material through mechanical testing is inconclusive. Nonetheless, the data points obtained in the unstable crack growth regime shows continuity with the unstable crack growth rates obtained from mechanical testing.

3.3.3. Fracture surface Investigation

The fracture surfaces of the failed fatigue samples were investigated using SEM at room temperature to identify key fracture surface characteristics. All SEM images were taken in the steady crack growth rate regime (i.e., after pre-cracking and before unstable crack growth). Fig. 17 shows the fracture surface after a mechanical fatigue crack growth experiment at M_s +45 °C for the SHT specimen Fig. 17b and c are magnified versions of the selected area (blue square) on Fig. 17a. Similarly, Fig. 17e, f, and 17g are the fracture profile and the selected magnified area (blue square) after a mechanical fatigue crack growth experiment at M_s +45 °C of the specimen in PA condition. The blue squares were placed on plane sections of both fracture surfaces to contrast fracture features with consistent area selection criteria. From Fig. 17c and g, it is evident that more plasticity occurs in the SHT specimen during crack growth. In the peak aged condition, parallel striations indicative of cleavage fracture can be observed. It is hypothesized that nanoprecipitates suppress transgranular dislocation motion in the austenitic phase of the PA condition. On the other hand, microvoid coalescence can be observed in the SHT specimen (Fig. 17c and d) due to the dislocation plasticity during cycling. Finally, magnified selected areas (green squares) from rough fracture surface locations are shown in Fig. 17d for SHT and 17h for PA conditions. In these SEM images, a higher density of microvoids and striations are observed for the SHT and PA specimens, respectively, which further confirms the presence of plasticity in SHT material and the interference of dislocation formation in the PA material.

4. Summary and conclusions

In the present study, the effects of coherent H-phase nanoprecipitates on the fracture and fatigue crack growth properties of a Ni-rich

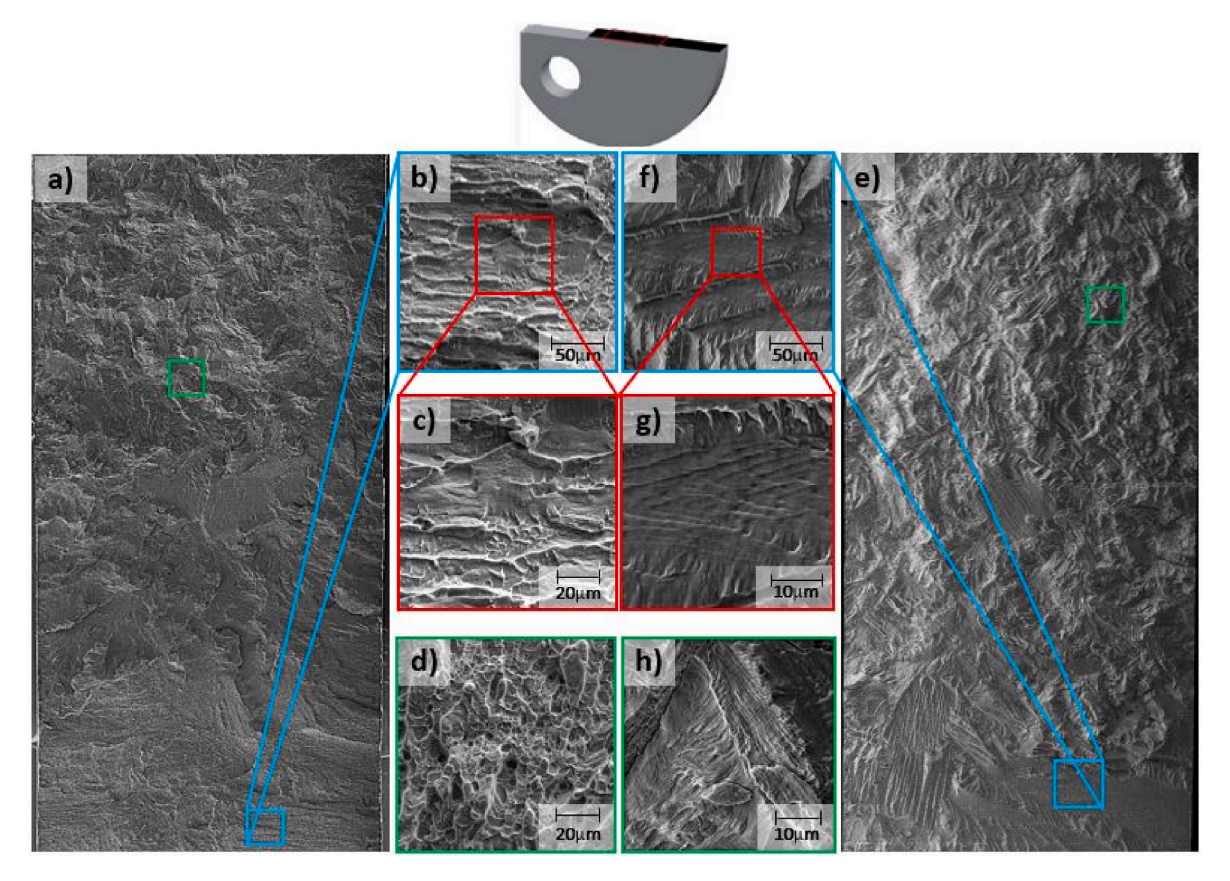


Fig. 17. (a) Fracture surface of the SHT specimen after the mechanical crack growth experiment shown in Fig. 8, (b) selected area on the fracture surface marked by blue square in (a), (c) magnified view of the selected area in (b), and (d) magnified view of another location on the SHT fracture surface. (e) Fracture surface of the PA specimen after the mechanical crack growth experiment shown in Fig. 8, (f) selected area on the fracture surface marked by blue square in (e), (g) magnified view of the selected area in (f), and (h) magnified view of another location on the PA fracture surface. (For interpretation of the references to colour in this figure legend, the reader is referred to the Web version of this article.)

 $Ni_{50.3}Ti_{29.7}Hf_{20}$ HTSMA were investigated. Fracture toughness tests were conducted (i) in the martensite phase, (ii) across martensitic transformation, and (iii) in the austenite phase. The fracture toughness for homogeneous and nanoprecipitation-hardened NiTiHf increased in the presence of stress-induced martensitic transformation, case (ii). However, a much larger increase in fracture toughness was attained in the SHT condition since precipitates lower the capability of $Ni_{50.3}Ti_{29.7}Hf_{20}$ to release the stresses at the crack tip. On the other hand, the fracture toughness of stable austenite in the PA condition is larger than the stable austenite fracture toughness in the SHT condition. This is expected due to the precipitation hardening of the material at high temperatures.

Mechanical and actuation fatigue crack growth rates were also determined upon martensitic transformation in both microstructures. A single Paris Law type ($\Delta J vs. \frac{da}{dN}$) curve was obtained from isobaric actuation and near-isothermal mechanical loading paths for the PA material. The same experiments were performed in SHT NiTiHf but were deemed inconclusive since its actuation crack growth rates could only be determined at the unstable crack growth regime of the Paris curve. Nonetheless, $(\Delta J vs. \frac{da}{dN})$ continuity alludes to the potential prediction of actuation crack growth rates utilizing mechanical fatigue crack growth rate. In actuation fatigue crack growth tests for SHT material at loads lower than 0.5 P_{max} , the buildup of crack tip plasticity dominated the driving force, resulting in asymptotically decreasing Δ CMOD. This can be explained by the relatively large residual strain left after an actuation cycle in the SHT condition that is not present in the PA condition. This hypothesis was further underscored by the difference in fracture surface features of the fatigued samples between the SHT and PA conditions—the SHT fracture surface displayed more evidence of ductile rupture than the PA condition.

In general, the experiments suggest that nanoprecipitates, needed to stabilize functional fatigue behavior of NiTiHf HTSMAs, reduce the fatigue crack growth threshold and increase the steady crack growth rate, negatively impacting their damage tolerance. This work further reinforced the ability to relate mechanical and actuation fatigue crack growth rates using ΔJ as the fatigue driving force and that mechanical fatigue crack growth responses can be used to estimate the actuation fatigue crack growth rates.

Based on the aforementioned results, the major findings and conclusions can be summarized as follows:

- Precipitates play an important role in both actuation and mechanical fatigue crack growth. In mechanical crack growth, SHT (precipitate-free) specimens exhibited a larger ΔJ_{th} (\sim 0.7 kJ/m²) compared to PA specimens (\sim 0.14 kJ/m²). Also, SHT material experienced lower crack growth rates in the steady crack growth rate regime of the Paris curve. This is attributed to the large plasticity buildup at the crack tip for SHT NiTiHf. Plasticity buildup was also observed in SHT specimens during actuation fatigue tests; crack growth during actuation cycling hinges on the capacity of the bias load to trigger crack growth past the inelastic area ahead of the crack tip.
- Martensitic transformation acts as a toughness enhancement mechanism resulting in stable crack growth in the SHT material under overload fracture. In the PA material, the creation of new surfaces seems to be more energetically favorable than phase transformation resulting in unstable crack growth at least for the crack configuration and loading conditions tested.

- A unified Paris-law curve was constructed from mechanical and actuation fatigue crack growth experiments on the precipitationhardened material. A unified description of actuation and mechanical fatigue crack growth rates can save cost and time by predicting crack growth rates under actuation loading with faster mechanical tests.
- Although nanoprecipitates are needed to stabilize actuation fatigue behavior of NiTiHf HTSMAs, they reduce the fatigue crack growth threshold and increase the steady crack growth rate during mechanical fatigue, negatively impacting their damage tolerance.

Given these findings, this work ultimately aids in elucidating the response of $\mathrm{Ni}_{50.3}\mathrm{Ti}_{29.7}\mathrm{Hf}_{20}$ HTSMA across martensitic transformation for SHT and PA specimens, making it possible to compare responses and accordingly select an optimum microstructure for different actuator applications. In addition, it supports the possibility of a unified relationship for mechanical and actuation fatigue crack growths for multiple microstructures.

CRediT authorship contribution statement

Benjamin Young: Writing – original draft, Visualization, Validation, Methodology, Investigation, Formal analysis, Data curation. Roberto Orrostieta: Writing - original draft, Visualization, Validation, Methodology, Investigation, Formal analysis, Data curation. Behrouz Haghgouyan: Methodology, Formal analysis, Data curation. Dimitris C. Lagoudas: Writing - review & editing, Supervision, Project administration, Formal analysis, Conceptualization. T. Baxevanis: Writing review & editing, Supervision, Methodology, Investigation, Funding acquisition, Formal analysis, Conceptualization. Ibrahim Karaman: Writing - review & editing, Supervision, Resources, Project administration, Methodology, Investigation, Funding acquisition, Conceptualization.

Declaration of competing interest

The authors declare that they have no known competing financial interests or personal relationships that could have appeared to influence the work reported in this paper.

Data availability

Data will be made available on request.

Acknowledgements

This study was supported by the National Science Foundation under Grants no. CMMI-1917367, CMMI-1917441. IK acknowledges the support from the National Science Foundation under Grant no. DMR-2004752.

References

- D.J. Hartl, D.C. Lagoudas, Aerospace applications of shape memory alloys, Proc. Inst. Mech. Eng. G J. Aerosp. Eng. 221 (4) (2007) 535–552.
- [2] J. Ma, I. Karaman, R.D. Noebe, High temperature shape memory alloys, Int. Mater. Rev. 55 (5) (2010) 257–315.
- [3] T. Umale, D. Salas, B. Tomes, R. Arroyave, I. Karaman, The effects of wide range of compositional changes on the martensitic transformation characteristics of NiTiHf shape memory alloys. Scripta Mater. 161 (2019) 78–83.
- [4] D. Canadinc, W. Trehern, H. Ozcan, C. Hayrettin, O. Karakoc, I. Karaman, F. Sun, Z. Chaudhry, On the deformation response and cyclic stability of Ni50Ti35Hf15 high temperature shape memory alloy wires, Scripta Mater. 135 (2017) 92–96.
- [5] O. Karakoc, K.C. Atli, O. Benafan, R.D. Noebe, I. Karaman, Actuation fatigue performance of NiTiZr and comparison to NiTiHf high temperature shape memory alloys, Mater. Sci. Eng. a-Struct. Mater. Propert. Microstruct. Process. (2022) 829.
 [6] N. Babacan, M. Bilal, C. Hayrettin, J. Liu, O. Benafan, I. Karaman, Effects of cold
- [6] N. Babacan, M. Bilal, C. Hayrettin, J. Liu, O. Benafan, I. Karaman, Effects of cold and warm rolling on the shape memory response of Ni₅₀Ti₃₀Hf₂₀ high-temperature shape memory alloy, Acta Mater. 157 (2018) 228–244.

- [7] M. Belbasi, M. Salehi, Influence of chemical composition and melting process on hot rolling of NiTiHf shape memory alloy, J. Mater. Eng. 23 (2014) 2368–2372.
- [8] O. Benafan, in: Deformation and Phase Transformation Processes in Polycrystalline NiTi and NiTiHf High Temperature Shape Memory Alloys, University of Central Florida, 2012. Ph.D. Dissertation.
- [9] O. Benafan, R.D. Noebe, S.A. Padula, R. Vaidyanathan, Microstructural response during isothermal and isobaric loading of a precipitation-strengthened Ni29.7-Ti-20Hf high-temperature shape memory alloy, Metall. Mater. Trans. 43 (12) (2012) 4539–4552.
- [10] G. Bigelow, A. Garg, S. Padula Ii, D. Gaydosh, R. Noebe, Load-biased shapememory and superelastic properties of a precipitation strengthened hightemperature Ni50. 3Ti29. 7Hf20 alloy, Scripta Mater. 64 (8) (2011) 725–728.
- [11] A. Evirgen, Microstructural characterization and shape memory response of Ni-Rich NiTiHf and NiTiZr high temperature Shape Memory Alloys, in: Department of Materials Science and Engineering, Texas A&M University, 2014.
- [12] A. Evirgen, F. Basner, I. Karaman, R.D. Noebe, J. Pons, R. Santamarta, Effect of aging on the martensitic transformation characteristics of a Ni-rich NiTiHf high temperature shape memory alloy, Funct. Mater. Lett. 5 (4) (2012) 1250038.
- [13] A. Evirgen, I. Karaman, R.D. Noebe, R. Santamarta, J. Pons, Effect of precipitation on the microstructure and the shape memory response of the Ni_{50.3}Ti_{29.7}Zr₂₀ high temperature shape memory alloy, Scripta Mater. 69 (5) (2013) 354–357.
- [14] A. Evirgen, I. Karaman, R. Santamarta, J. Pons, C. Hayrettin, R.D. Noebe, Relationship between crystallographic compatibility and thermal hysteresis in Nirich NiTiHf and NiTiZr high temperature shape memory alloys, Acta Mater. 121 (2016) 374–383.
- [15] A. Evirgen, I. Karaman, R. Santamarta, J. Pons, R. Noebe, Microstructural characterization and shape memory characteristics of the Ni50. 3Ti34. 7Hf15 shape memory alloy, Acta Mater. 83 (2015) 48–60.
- [16] A. Evirgen, J. Pons, I. Karaman, R. Santamarta, R.D. Noebe, H-Phase precipitation and martensitic transformation in Ni-rich Ni-Ti-Hf and Ni-Ti-Zr high-temperature shape memory alloys, Shape Memory and Superelasticity 4 (1) (2018) 85–92.
- [17] C. Hayrettin, Actuation fatigue and fracture of shape memory alloys, in: Department of Materials Science and Engineering, Texas A&M University, 2017.
- [18] C. Hayrettin, O. Karakoc, I. Karaman, J.H. Mabe, R. Santamarta, J. Pons, Two way shape memory effect in NiTiHf high temperature shape memory alloy tubes, Acta Mater. 163 (2019) 1–13.
- [19] H.E. Karaca, E. Acar, H. Tobe, S.M. Saghaian, NiTiHf-based shape memory alloys, Mater. Sci. Technol. 30 (13) (2014) 1530–1544.
- [20] O. Karakoc, A. Demblon, R.W. Wheeler, D.C. Lagoudas, I. Karaman, Effects of testing parameters on the fatigue performance NiTiHf high temperature shape memory alloys. in: AIAA Scitech 2019 Forum, 2019.
- [21] O. Karakoc, C. Hayrettin, D. Canadinc, I. Karaman, Role of applied stress level on the actuation fatigue behavior of NiTiHf high temperature shape memory alloys, Acta Mater. 153 (2018) 156–168.
- [22] O. Karakoc, C. Hayrettin, A. Evirgen, R. Santamarta, D. Canadinc, R.W. Wheeler, S. J. Wang, D.C. Lagoudas, I. Karaman, Role of microstructure on the actuation fatigue performance of Ni-Rich NiTiHf high temperature shape memory alloys, Acta Mater. 175 (2019) 107–120.
- [23] B. Kockar, I. Karaman, J. Kim, Y. Chumlyakov, A method to enhance cyclic reversibility of NiTiHf high temperature shape memory alloys, Scripta Mater. 54 (12) (2006) 2203–2208.
- [24] S.M. Russell, F. Sczerzenie, Engineering considerations in the application of NiTiHf and NiAI as practical high-temperature shape memory alloys, MRS Proceedings 360 (1994) 455.
- [25] S.M. Saghaian, H.E. Karaca, M. Souri, A.S. Turabi, R.D. Noebe, Tensile shape memory behavior of Ni_{50.3}Ti_{29.7}Hf₂₀ high temperature shape memory alloys, Mater. Des. 101 (2016) 340–345.
- [26] S.M. Saghaian, H.E. Karaca, H. Tobe, M. Souri, R. Noebe, Y.I. Chumlyakov, Effects of aging on the shape memory behavior of Ni-rich Ni_{50.3}Ti_{29.7}Hf₂₀ single crystals, Acta Mater. 87 (2015) 128–141.
- [27] R. Santamarta, R. Arróyave, J. Pons, A. Evirgen, I. Karaman, H.E. Karaca, R. D. Noebe, TEM study of structural and microstructural characteristics of a precipitate phase in Ni-rich Ni-Ti-Hf and Ni-Ti-Zr shape memory alloys, Acta Mater. 61 (16) (2013) 6191–6206.
- [28] D. Shukla, R.D. Noebe, P. Stebner Aaron, Empirical study of the multiaxial, thermomechanical behavior of NiTiHf shape memory alloys, in: NASA/TM—2013-216619, National Aeronautics and Space Administration, 2013.
- [29] G.S. Bigelow, A. Garg, O. Benafan, R.D. Noebe, S.A.P. Ii, D.J. Gaydosh, Development and testing of a Ni50.5Ti27.2Hf22.3 high temperature shape memory alloy, Materialia 21 (2022).
- [30] K.C. Atli, I. Karaman, R.D. Noebe, G. Bigelow, D. Gaydosh, Work production using the two-way shape memory effect in NiTi and a Ni-rich NiTiHf high-temperature shape memory alloy, Smart Mater. Struct. 24 (12) (2015).
- [31] S.W. Robertson, A.R. Pelton, R.O. Ritchie, Mechanical fatigue and fracture of Nitinol, Int. Mater. Rev. 57 (1) (2012) 1–36.
- [32] T. Baxevanis, D.C. Lagoudas, Fracture mechanics of shape memory alloys: review and perspectives, Int. J. Fract. 191 (1–2) (2015) 191–213.
- [33] G.Z. Kang, D. Song, Review on structural fatigue of NiTi shape memory alloys: pure mechanical and thermo-mechanical ones, Theoret. Appl. Mech. Lett. 5 (6) (2015) 245–254.
- [34] K. Nargatti, S. Ahankari, Advances in enhancing structural and functional fatigue resistance of superelastic NiTi shape memory alloy: a Review, J. Intell. Mater. Syst. Struct. 33 (4) (2022) 503–531.
- [35] O. Karakoc, C. Hayrettin, M. Bass, S.J. Wang, D. Canadinc, J.H. Mabe, D. C. Lagoudas, I. Karaman, Effects of upper cycle temperature on the actuation

- fatigue response of NiTiHf high temperature shape memory alloys, Acta Mater. 138
- [36] O. Akgul, H.O. Tugrul, B. Kockar, Effect of the cooling rate on the thermal and thermomechanical behavior of NiTiHf high-temperature shape memory alloy, J. Mater. Res. 35 (12) (2020) 1572–1581.
- [37] A. Demblon, O. Karakoc, J. Sam, D. Zhao, K.C. Atli, J.H. Mabe, I. Karaman, Compositional and microstructural sensitivity of the actuation fatigue response in NiTiHf high temperature shape memory alloys, Mater. Sci. Eng. a-Struct. Mater. Propert. Microstruct. Process. (2022) 838.
- [38] B. Young, B. Haghgouyan, D.C. Lagoudas, I. Karaman, Effect of temperature on the fracture toughness of a NiTiHf high temperature shape memory alloy, Shape Memory and Superelasticity 5 (4) (2019) 362–373.
- [39] B. Haghgouyan, B. Young, I. Karaman, D.C. Lagoudas, Fracture toughness of martensitic NiTiHf high-temperature shape memory alloy, SPIE Smart Structures + Nondestructive Evaluation 10968 (2019). SPIE.
- [40] M. Ekiciler, B. Kockar, Crack growth behavior during actuation cycling of hot extruded and annealed Ni50Ti30Hf20 high temperature shape memory alloys, Smart Mater. Struct. 31 (9) (2022).
- [41] B. Haghgouyan, B. Young, S. Picak, T. Baxevanis, I. Karaman, D.C. Lagoudas, A unified description of mechanical and actuation fatigue crack growth in shape memory alloys, Acta Mater. 217 (2021) 117155.
- [42] M.M. Hasan, T. Baxevanis, Structural fatigue and fracture of shape memory alloy actuators: current status and perspectives, J. Intell. Mater. Syst. Struct. 33 (12) (2022) 1475–1486.
- [43] T. Baxevanis, D.C. Lagoudas, Fracture mechanics of shape memory alloys: review and perspectives, Int. J. Fract. 191 (1) (2015) 191–213.
- [44] B. Haghgouyan, C. Hayrettin, T. Baxevanis, I. Karaman, D.C. Lagoudas, Fracture toughness of NiTi-Towards establishing standard test methods for phase transforming materials, Acta Mater. 162 (2019) 226–238.
- [45] J. Makkar, T. Baxevanis, Notes on the experimental measurement of fracture toughness of shape memory alloys, J. Intell. Mater. Syst. Struct. 31 (3) (2020) 475–483.
- [46] A. Evirgen, F. Basner, I. Karaman, R.D. Noebe, J. Pons, R. Santamarta, Effect of aging on the martensitic transformation characteristics of a Ni-rich NiTiHf high temperature shape memory alloy, Funct. Mater. Lett. 5 (4) (2012) 1250038.
- [47] ASTM Standard E1820, Standard Test Method for Measurement of Fracture Toughness, ASTM International, 2014.
- [48] J.C. Newman, Stress-intensity factors and crack-opening displacements for round compact specimens, Int. J. Fract. 17 (6) (1981) 567–578.
- [49] ASTM Standard E399, Standard Test Method for Linear-Elastic Plane-Strain Fracture Toughness K_{Ic} of Metallic Materials, ASTM International, 2011.

- [50] ASTM Standard E647, Standard Test Method for Measurement of Fatigue Crack Growth Rates, ASTM International, 2015.
- [51] S. Jape, B. Young, B. Haghgouyan, C. Hayrettin, T. Baxevanis, D.C. Lagoudas, I. Karaman, Actuation-Induced stable crack growth in near-equiatomic nickeltitanium shape memory alloys: experimental and numerical analysis, Int. J. Solid Struct. 221 (2021) 165–179.
- [52] O. Benafan, A. Garg, R.D. Noebe, G.S. Bigelow, S.A. Padula, D.J. Gaydosh, N. Schell, J.H. Mabe, R. Vaidyanathan, Mechanical and functional behavior of a Nirich Ni_{50.3}Ti_{29.7}Hf₂₀ high temperature shape memory alloy, Intermetallics 50 (2014) 94–107.
- [53] H. Karaca, S. Saghaian, G. Ded, H. Tobe, B. Basaran, H. Maier, R. Noebe, Y.J.A. M. Chumlyakov, Effects of nanoprecipitation on the shape memory and material properties of an Ni-rich NiTiHf high temperature shape memory alloy, Acta Mater. 61 (19) (2013) 7422–7431.
- [54] S. Miyazaki, T. Imai, Y. Igo, K. Otsuka, Effect of cyclic deformation on the pseudoelasticity characteristics of Ti-Ni alloys, Metall. Trans. A 17 (1) (1986) 115–120.
- [55] T. Simon, A. Kröger, C. Somsen, A. Dlouhy, G. Eggeler, On the multiplication of dislocations during martensitic transformations in NiTi shape memory alloys, Acta Mater. 58 (5) (2010) 1850–1860.
- [56] S.M. Saghaian, H.E. Karaca, H. Tobe, J. Pons, R. Santamarta, Y.I. Chumlyakov, R. D. Noebe, Effects of Ni content on the shape memory properties and microstructure of Ni-rich NiTi-20Hf alloys, Smart Mater. Struct. 25 (9) (2016).
- [57] S.W. Robertson, A. Mehta, A.R. Pelton, R.O. Ritchie, Evolution of crack-tip transformation zones in superelastic Nitinol subjected to in situ fatigue: a fracture mechanics and synchrotron X-ray microdiffraction analysis, Acta Mater. 55 (18) (2007) 6198–6207.
- [58] B. Amin-Ahmadi, J.G. Pauza, A. Shamimi, T.W. Duerig, R.D. Noebe, A.P. Stebner, Coherency strains of H-phase precipitates and their influence on functional properties of nickel-titanium-hafnium shape memory alloys, Scripta Mater. 147 (2018) 83–87.
- [59] A.P. Iliopoulos, J.C. Steuben, T. Kirk, T. Baxevanis, J.G. Michopoulos, D. C. Lagoudas, Thermomechanical failure response of notched NiTi coupons, Int. J. Solid Struct. 125 (2017) 265–275.
- [60] S. Jape, T. Baxevanis, D.C. Lagoudas, Stable crack growth during thermal actuation of shape memory alloys, Shape Memory and Superelasticity 2 (1) (2016) 104–113.
- [61] H. Akamine, A. Heima, Y. Soejima, M. Mitsuhara, M. Nishida, Where and when are dislocations induced by thermal cycling in Ti-Ni shape memory alloys? Acta Mater. 244 (2023).